Multi-dimensional entanglement generation with multi-core optical fibers

Generación de entrelazamiento multidimensional con fibras ópticas multi-núcleos

by

Ítalo Ignacio Machuca Flores

Thesis submitted for the degree of
Ph.D. in Physical Sciences

Department of physics
Universidad de Concepción

Examining Committee Membership

The following served on the Examining Committee for this thesis.

Supervisor(s): Gustavo Moreira Lima,
Professor, Physics departament,
Universidad de Concepción

External examiner: Gustavo Cañas Cardona,
Professor, Dept. of science,
University of Bio Bio

Internal member: Esteban Sepúlveda,
Professor, Physics departament,
Universidad de Concepción

Internal Member: Stephen Walborn,
Professor, Dept. of physics,
University of Concepción

Abstract

The common threads of my work in the Ph.D. was entanglement sources and the work and the works that served as an experimental basis are [20, 47]. Here, prove partially entangled state (PES) in quantum information protocols Bell inequality, Self-testing and Randomness certification. It was that the state with more entanglement have better performance in protocols and that nonlocality can be without additional measurements. This knowledge was used to prepare the main work of this thesis.
An source of entanglement pointing to the growing in classical optics and telecommunications. In this regard, advances in multiplexing optical communications channels have also been pursued for the generation of multi-dimensional quantum states (qudits), since their use is advantageous for several quantum information tasks. One current path leading in this direction is through the use of space-division multiplexing multi-core optical fibers, which provides a new platform for efficiently controlling path-encoded qudit states. Here we report on a parametric down-conversion source of entangled qudits that is fully based on (and therefore compatible with) state-of-the-art multi-core fiber technology. The source design uses modern multi-core fiber beam splitters to prepare the pump laser beam as well as measure the generated entangled state, achieving high spectral brightness while providing a stable architecture. In addition, it can be readily used with any core geometry, which is crucial since widespread standards for multi-core fibers in telecommunications have yet to be established. Our source represents an important step towards the compatibility of quantum communications with the next-generation optical networks.

Acknowledgements

Debo partir agradeciendo a quienes son parte de este camino mucho antes del doctorado. Mi familia es la base de haber podido llegar hasta aquí, mis padres Victor Machuca y Marcela Flores, hermano Martín, abuelos Tito, Ita, Erasmo y Linda, Silvia, tíos, primos, padrinos. Aportando con cualquier muestra de afecto y contención ayudaron a que no bajara de este camino, por lo que no dimensionan lo que me ayudaron. Los amigos, nada más con mencionarlos me dan ganas de agradecer a cada uno por las conversaciones de todo tipo, desde lo académico hasta lo más banal. Sirvió un montón para descansar (o escaparme) de la tensión. A mis profesores, Al profesor Lima (Glima) que confió en mi sin conocerme, Esteban que siempre hace el ambiente en el laboratorio más agradable (según el), Gustavo Cañas retando al mundo y ayudando al mismo tiempo, Sthepen por la ayuda constante, Daniel y Santiago que siempre estaban dispuestos a trabajar, al equipo del laboratorio en general que son grandísimas personas. Siempre agradeceré la ayuda académica, pero más importante la ayuda personal y el ambiente de amistad que me hicieron sentir.
Se que en un camino como este, siempre uno se queda corto con las palabras o personas que menciona. A cada uno uno le debo más de lo que me ha entregado y feliz de poder tener este núcleo cerca mio.

Dedication

Victor, Marcela y Martín esto es para ustedes.

Nadie se da cuenta de que se trata el mundo, y no importa. Explora el mundo, casi todos es interesante si profundizas en ello.

-Richard P. Feynman

Table of Contents

List of Tables

List of Figures

Chapter 1

Introduction

The study of the quantum physics was born at the beginning of $20th$, century with ultraviolet catastrophe [1] and from there a series of efforts were unleashed to understand physics at the particle level. Einstein, Podolsky and Rosen continued recognizing this feature of new physics, that implies the global state of a composite system [2]. This phenomenon, which was originally named *spooky* by Einstein or *Verschränkung* by Schrödinger, was later called entanglement.
In 1964 J. Bell[1], product of your work, accepted the EPR conclusion and formalized the idea of deterministic world in terms of the local hidden variable (LHVM) [3]. He proved if a the experiment employ a quantum state the Bell's inequalities are violated, i.e. the probabilities outcomes has statistical correlations and evolved a bipartite quantum state. This, is a feature that make impossible explain quantum mechanic with classical formalism. This, gave rise to experiments, but the first convincingly was Alain Aspect, showing a violation test of Bell inequalities [5, 6]. This continued grow, generating maximal entangled stated (MES) [95] and proving Bell inequality, partially entangled states (PES) [20] or proving that the quantum state of high dimension are better option in some protocols that the smaller ones [41]. This is one area that explode this work, the quantum entanglement state in high dimension, the other arm is the communications.

The task of processing quantum information from quantum state has seen growth since Richard Feynman[2] mention the use of quantum computers to simulate physical system [8]. Using quantum states, like those mentioned in the previous paragraph, an improvement is obtained over classical system. For example, for classical computer is *easy* multiply prime numbers, but the inverse process is complicated and a quantum solution is Short algorithm [4]. Another example, is the Grover's algorithm [7], which can improve the search for an item in quadratic form[3], exploiting a property that has no analogy in the classical version, such as phase amplification. The last example, pointed to communication, is use quantum physics for security, where it's taken advantage of the quantum state cannot be cloned

[1] John Stewart Bell, Northern Ireland physicist, 1928-1990.

[2] Richard Phillips Feynman, American physicist, 1918-1988.

[3] In classical computer the range for requirements is between $N/2$ to N, but a quantum computer is roughly $\sqrt{N}$.

[9]. This is the base for quantum protocol Quantum Key Distribution (QKD), which distributed random private keys between two parties [11]. The latter, is part of the are called quantum communication.
When materializing communications, the continuous increase in demand for the transmission of information must be considered. Here, the optical fiber play a important role for his high bandwidth support [99]. Some technologies ware implemented in order to improve the capacities and transmission, as erbium doped fiber amplifier [97] or wavelength division multiplexing (WDM) [98]. The last decade, the technology drive towards maintaining the bandwidth growth is called space-division multiplexing (SDM), and consist in use the transversal spatial properties of the light, multiplexing information and allowing keep the growing in data capacity [32].

In this thesis, was used the quantum physics and spatial division multiplexing for implemented a photonic quantum entanglement source. The quantum state is encoded in path, that provide from a multicore fiber of four core, showing high compatibility with SDM multicore technology. The use of this kind of fiber add to source the possibility of identify independently each core and better behavior of relative phases. Furthermore, the possibility of implemented a protocols in high dimension and based fully on SDM technology. Knowing on the one hand, that quantum state in d-dimensional offer better result and the compatibility can be used for next-generation SDM optical networks.

Chapter 2

Theoretical framework

The theoretical chapter shows the fundamental pillars of this thesis. First is a review of quantum mechanics where the key ideas, physical and mathematical, are stated. Second is quantum information theory, with the mathematical and graphical representation of quantum bits and quantum dits.

2.1 Quantum mechanics

2.1.1 Introduction to quantum mechanics

Quantum mechanics play a principal role in understand natural phenomena, but in atomic or subatomic scale. This physics area came to explain properties of atoms [24], electron diffraction [28], etc. that cannot explain with other physics theory. This new concepts and ideas, in the beginning of the twentieth, marked a turning point or also called as quantum revolution, challenging the classical physics in different points. Here, we show the vocabulary and ideas for the futures chapters.

To start with the description, let's take Broglie's[1] hypothesis [13] and gives rise to the following formulation.

- The quantum state of a particle is characterize by a wave function $\psi(\vec{r}, t)$, which contain all the information it is possible to obtain about the particle.
- $\psi(\vec{r}, t)$ is interpreted as a probability amplitude of the particle's presence. Is the possible position of a particle, the probability $\mathcal{P}(\vec{r}, t)$ of the particle at time t, in a $d^3r = dxdydz$ volume. Then $|\psi(\vec{r}, t)|$ is interpreted as probability density.
- The principle of spectral decomposition applies to the measurement of an arbitrary physical quantity:

[1] Louis Victor Pierre Raymond, 7th Duc de Broglie. French physicist, 1892-1987.

- The found result must belong to a set of outcomes $\{a\}$, called eigenvalues.

- Each eigenvalues is associated to an eigenstate, in this case, eigenfuction $\psi(\vec{r},t)$.

- For any $\psi(\vec{r},t)$ the probability $\mathcal{P}$ of finding the eigenvalue a for a measurement at time t_o is found decomposing $\psi(\vec{r},t)$ in terms the $\psi_a(\vec{r})$

$$\psi(\vec{r},t_0)=\sum_a \psi_a(\vec{r}). \tag{2.1}$$

Then

$$\mathcal{P}_a=\frac{|c_a|^2}{\sum_a |c_a|^2}, \tag{2.2}$$

with this the probabilities are equal to 1, i.e $\sum_a \mathcal{P}_a=1$.

Finally, in this introduction, mentioned for a system for a particle, the total probability of finding the particle anywhere in space is:

$$\int d\mathcal{P}(\vec{r},t)=1 \tag{2.3}$$

and it is concluded that

$$\int |\psi(\vec{r},t)|^2 d^3r=1. \tag{2.4}$$

2.1.2 The mathematical tools for quantum mechanics

Wave function space

In the previous chapter, the equation (2.4) shows the probabilistic interpretation of the wave function. These functions are well-behaved[2] and belong to infinite-dimensional space. Then, we can consider the function $\psi(\vec{r})$ which is everywhere defined, in other words, is a continue function, infinitely differentiable and living in a function space. We will call $\mathfrak{F}$ the space of wave functions composed of regular functions.

As a first step, we show if $\psi(\vec{r})_1$ and $\psi(\vec{r})_2 \in \mathfrak{F}$ then:

$$\Psi(\vec{r})=\lambda_1\psi(\vec{r})_1+\lambda_2\psi(\vec{r})_2 \quad \in \quad \mathfrak{F} \tag{2.5}$$

[2]Square-integrable function: This set is called L^2, and is real or complex function in which the integral of square of the absolute value is finite.

where λ_1 and λ_2 are two complex numbers.
Now, we consider two element of $\mathfrak{F}$, $\psi(\vec{r})$ and $\varphi(\vec{r})$, result a complex number, denoted by (φ, ψ). The definition is

$$(\varphi, \psi) = \int \varphi^*(\vec{r})\psi(\vec{r})d^3r. \tag{2.6}$$

This formula is called *scalar product* and is important the order of factors. Now taking the equation (2.6) follow this definitions:

$$\begin{aligned} (\varphi, \psi) &= (\psi, \varphi)^* && (2.7)\\ (\varphi, \lambda_1\psi + \lambda_2\psi) &= \lambda_1(\varphi, \psi_1) + \lambda_2(\varphi, \psi_2) && (2.8)\\ (\lambda_1\varphi_1 + \lambda_2\varphi_2, \psi) &= \lambda_1^*(\varphi_1, \psi) + \lambda_2^*(\varphi_2, \psi) && (2.9) \end{aligned}$$

If the scalar product is zero, φ and ψ are orthogonal and is a positive real number if is between the same wave function

$$(\psi, \psi) = \int |\psi(\vec{r})|^2 d^3r. \tag{2.10}$$

So far, we have shown in the continuous case, but now we can consider a set orthonormal[3] of $\mathfrak{F}$ with discrete elements, where the index $i = 1, 2, 3, ..., n$:

$$u_1, u_2, ..., u_i \quad \in \quad \mathfrak{F}.$$

It constitutes a basis for $\psi(\vec{r}) \in \mathfrak{F}$ and can be expanded in terms of $u_i(\vec{r})$:

$$\psi(\vec{r}) = \sum_i c_i u_i(\vec{r}), \tag{2.11}$$

based in the equation (2.11) we can define how obtain the specific element c_j of $\psi(\vec{r})$

$$\begin{aligned} (u_j, \psi) &= \left(u_j, \sum_i c_i u_i\right) = \sum_i c_i (u_j, u_i) \\ (u_j, \psi) &= \sum_i c_i \delta_{ij} = c_j. && (2.12) \end{aligned}$$

For the scalar product in terms of the components we can follow a similar process. Let $\varphi(\vec{r})$ and $\psi(\vec{r})$ are two wave functions which can be expanded as follow:

$$\begin{aligned} \varphi(\vec{r}) &= \sum_i b_i u_i(\vec{r}) \\ \psi(\vec{r}) &= \sum_j c_j u_j(\vec{r}), && (2.13) \end{aligned}$$

[3]The set is orthonormal if $(u_i, u_j) = \int u_i^* u_j d^3r = \delta_{ij}$

and their scalar product can be calculate by element in equation (2.13):

$$(\varphi, \psi) = \sum_i b_i^* c_i \tag{2.14}$$

$$(\psi, \psi) = \sum_i |c_i|^2. \tag{2.15}$$

In (2.14) is scalar product between two different wave function and (2.15) is between the same wave function and is the square modulus of coefficient.

Dirac notation

When we describe the function space and the probabilistic interpretation of $\psi(\vec{r})$, we said that is part of the square-integrable function. For this reason we defined the $\mathfrak{F}$-space, where the wave function can be represented in basis $\{u_i\}$ with different sets of components $\{c_i\}$ (with $i = 1, 2, ..., n$).
How could one think the elements of basis like coordinates in three dimensional space, now we can use similar approach. Then, we are going each quantum state of the particle will be characterized by state vector, belonging to the Hilbert space[4] $\mathcal{H}$, called state space of particle.

$$\psi(\vec{r}) \in \mathfrak{F} \leftrightarrow |\psi\rangle \in \mathcal{H}.$$

The Hilbert space is vectorial space of complex numbers (denoted by $\mathbb{C}$), where exist the sum and scalar product. The elements $|\cdot\rangle$ are called *Kets* and $\langle\cdot|$ are called *bras*. To this new notation approached is called Dirac notation[5].
Let the following kets $|a\rangle$, $|b\rangle$, $|c\rangle \in \mathcal{H}$ and z, $w \in \mathbb{C}$. These operation are satisfied

$$|a\rangle + |b\rangle = |b\rangle + |a\rangle\,, \tag{2.16}$$

$$|a\rangle + |0\rangle = |a\rangle\,, \tag{2.17}$$

$$|a\rangle + |-a\rangle = |0\rangle\,, \tag{2.18}$$

$$z(|a\rangle + |b\rangle) = z\,|a\rangle + z\,|b\rangle\,, \tag{2.19}$$

$$(z + w)\,|a\rangle = z\,|a\rangle + w\,|a\rangle\,, \tag{2.20}$$

$$(zw)\,|a\rangle = z(w\,|a\rangle). \tag{2.21}$$

The scalar product in Dirac notation between the element is defined as $\langle a|b\rangle$. This inner product fulfills the following properties

$$\langle a|b\rangle = \langle b|a\rangle^*\,, \tag{2.22}$$

$$(|a\rangle\,, z\,|b\rangle + w\,|c\rangle) = z\,\langle a|b\rangle + w\,\langle a|c\rangle\,. \tag{2.23}$$

The $\langle a|a\rangle \geq 0$ always $\forall\ |a\rangle$, if $\langle a|a\rangle = 0$ then $|a\rangle = 0$ and other property is that $\langle a|b\rangle = 0$ the $|a\rangle$ and $|b\rangle$ are orthogonal vectors. The norm of the vector $|a\rangle$ is defined by

$$||\,|a\rangle\,|| = \sqrt{\langle a|a\rangle}. \tag{2.24}$$

[4]Named after the German mathematician David Hilbert, 1862-1943.
[5]Named after the British mathematician and physicist Paul Dirac, 1902-1984.

The details of vector representation of $|a\rangle$ is the following. Let $\{|u_i\rangle\}$ a basis, the ket $|a\rangle$ is represented by the set of its components, namely, $c_i = \langle u_i|a\rangle$. this components form a one column matrix.

$$|a\rangle = \begin{pmatrix} \langle u_1|a\rangle \\ \langle u_2|a\rangle \\ \vdots \\ \langle u_i|a\rangle \\ \vdots \end{pmatrix} \tag{2.25}$$

Analogously the bras representation is

$$\langle a| = (\langle u_1|a\rangle \quad \langle u_2|a\rangle \quad \cdots \quad \langle u_i|a\rangle \cdots) \tag{2.26}$$

2.1.3 Postulates of Quantum Mechanics

Whit a short stroke of quantum physics and the necessary mathematical elements, now we show the postulate in quantum mechanics. Are four postulates, where they join the physical system, the evolution of him, the measurement and types of state that particle can form [22].

State space

The first postulate make the link between the physical system and the state vector, namely, formalize the mathematical form of a quantum state.

Postulate 1. *Associated to any physical system is a complex vector space with the inner product, in Hilbert space, known as the state space of the system. The System is completely described by its state vector, which is a unit vector in the system's state vector.*

The state vector can be represent by $|\psi\rangle$ and fulfill the norm requirement, $\langle\psi|\psi\rangle = 1$, and by the equation (2.5) the sum belong the same space, so we can define the simplest quantum system with Dirac notation, the qubit[6]. Suppose $|0\rangle$ and $|1\rangle$ an orthonormal basis and arbitrary superposition is given by

$$|\psi\rangle = \alpha\,|0\rangle + \beta\,|1\rangle \tag{2.27}$$

where the component α and β must satisfy that $|\alpha|^2 + |\beta|^2 = 1$.

[6]The qubit or quantum bit is the analogy to the classical bit

Other way of representation the physical system is using the density operator or density matrix. The difference with the $|\psi\rangle$ is that here we need a set of states, $|\psi_i\rangle$ with the probability p_i. The density operator of the system is defined by:

$$\rho = \sum_{i=1}^{n} p_i \left|\psi_i\right\rangle \left\langle\psi_i\right| \tag{2.28}$$

Mention that, the dimension between $|\psi\rangle$ and ρ may be different. Other important characterization, so that they are physically accepted is following the theorem

Theorem 1. An operator ρ is a density operator to some ensemble $\{p_i \left|\psi_i\right\rangle\}$ is and if only it satisfies the conditions:

- The trace of $\rho = 1$. That is $Tr(\rho) = 1$.
- ρ is positive semi-definite operator. That is $\langle\psi| \rho |\psi\rangle \geq 0$.

The density operator has two classification, if there exist a ρ such that $\rho = |\psi\rangle \langle\psi|$, with just one ket-bra (or projector) is called pure state. In the case that the state is a sum of several projectors, the density operator is a *mixed of states*, called mixed state. The explicit form of ρ with the spectral decomposition is

$$\rho = \sum_{i=0}^{n} p_i \left|\phi_n\right\rangle \left\langle\phi_n\right|, \tag{2.29}$$

where the p_i are the normalized eigenvalues ($\sum p_i = 1$) and satisfy $0 \leq p_i \leq 1$.
The purity of state is calculable, and should be evaluated the trace of square density operator. The purity parameter is given by

$$\gamma = Tr(\rho^2) = \sum_{i=1}^{n} p_i^2 \left|\phi_i\right\rangle \left\langle\phi_i\right| = \sum_{i=1}^{n} p_i^2 \tag{2.30}$$

the parameter $\gamma \in [1/d, 1]$, where d is the dimension of Hilbert space of state. If the purity is 1 is a pure state and $1/d$ is a completely mixed state.

Evolution

The first postulate related the physical system wit the vector state, now we see how this state change in the time.

Postulate 2. *The evolution of closed quantum system is described by a unitary transformation. that is, the state $|\psi\rangle$ of the system at time t_1 is related to the state $\left|\psi'\right\rangle$ of the system at time t_2 by a unitary operator[7] U which depends only on times t_1 and t_2.*

$$\left|\psi(t_2)\right\rangle = U(t_1, t_2) \left|\psi_1\right\rangle. \tag{2.31}$$

[7] A matrix is said to be unitary if $UU^\dagger = \mathbb{I}$

In terms of the density operator the state with the operator evolution is

$$\rho(t_2) = U(t_2, t_1)\rho U(t_1, t_2)^\dagger. \tag{2.32}$$

Emphasize on the concept *closed system*, this mean that the state that does not interact with the environment.

Quantum measurement

After showing the state and their evolution, the next step is the measurement stage. The third postulate introduce the means for describing the effect of measurement on quantum system.

Postulate 3. *Quantum measurement are described by a collection $\{M_m\}$ of measurement operator. These are the operator acting on the state space of the system being measurement. The index m refers to the measurement outcomes that may occur in the experiment. If the state is $|\psi\rangle$ immediately before the measurement then the probability that result m occurs is given by*

$$p(m) = \langle\psi| M_m^\dagger M_m |\psi\rangle \tag{2.33}$$

and the state of the system after the measurement is

$$|\psi_m\rangle = \frac{M_m |\psi\rangle}{\sqrt{\langle\psi| M_m^\dagger M_m |\psi\rangle}}, \tag{2.34}$$

where the measurement operator satify the completeness relation

$$\sum_m^n M_m^\dagger M_m = \mathbb{I}. \tag{2.35}$$

The completeteness equation expresses the fact that probabilities sum to one:

$$\sum_m^n p(m) = \sum_m^n \langle\psi| M_m^\dagger M_m |\psi\rangle = 1, \tag{2.36}$$

the equation (2.36) is for all $|\psi\rangle$. To see explicit the postulate, we can show a example with the measurement of qubit in computational basis $\{|0\rangle, |1\rangle\}$. This example has two outcome defined by the two measurement operator $M_0 = |0\rangle\langle 0|$ and $M_1 = |1\rangle\langle 1|$. Note that the measurement operator is Hermitian, so $M_0^2 = M_0$, $M_1^2 = M_1$. Also is satisfy the completeness, $\mathbb{I} = M_0^\dagger M_0 + M_1^\dagger M_1 = M_0 + M_1$. The target state is $|\psi\rangle = \alpha|0\rangle + \beta|1\rangle$.
For obtain the outcome[8] 0 and 1 is

$$p(0) = \langle\psi| M_0^\dagger M_0 |\psi\rangle = \langle\psi| M_0 |\psi\rangle = |\alpha|^2 \tag{2.37}$$

$$p(1) = \langle\psi| M_1^\dagger M_1 |\psi\rangle = \langle\psi| M_1 |\psi\rangle = |\beta|^2 \tag{2.38}$$

[8]Represent the probability of obtain 0 or 1 after measurement.

and the state after measurement is

$$|\psi_{m=0}\rangle = \frac{M_0 |\psi\rangle}{|a|} = \frac{a|0\rangle}{|a|} \tag{2.39}$$

$$|\psi_{m=1}\rangle = \frac{M_1 |\psi\rangle}{|b|} = \frac{b|1\rangle}{|b|}. \tag{2.40}$$

This analysis is for pure state, for the mixed state case the density operator after measurement is

$$\rho_m = \frac{M_m \rho M_m}{Tr(M_m \rho)} \tag{2.41}$$

and the probability for m outcome is

$$p(m) = Tr(M_m \rho) \tag{2.42}$$

This postulate accounts for the core of the quantum physics. When realize a quantum measurement the system is altered (Unlike the classical mechanics) and the possible outcomes is a probability, although these have been prepared in the same way. So, in the quantum mechanics we need several repetitions of experiment, one test is not enough.

Composite systems

Finally, the last postulate describe the systems of two or more particle.

Postulate 4. *The state space of a composite physical system is the tensor product of the state spaces of the component physical systems. If the subsystems are numbered from* 1 *to n, the state space is*

$$\mathcal{H} = \mathcal{H}_1 \otimes \mathcal{H}_2 \otimes \cdots \otimes \mathcal{H}_n. \tag{2.43}$$

This compose Hilbert space is associate with the state $|\Psi\rangle$, where each element is defined by $\{|\psi_i\rangle\}$

$$|\Psi\rangle = |\psi_1\rangle \otimes |\psi_2\rangle \otimes ... \otimes |\psi_n\rangle \tag{2.44}$$

if the estate $|\Psi\rangle$ can be write like equation (2.44) is called separable state, otherwise is a entangled state.
This kind of state are widely used en quantum teleportation [12], quantum cryptography [14] and violations of Bell's inequality [20] . A example is *Bell state* and are the maximally entangled state.

$$\left|\psi^{\pm}\right\rangle = \frac{1}{\sqrt{2}} \left(|01\rangle \pm |10\rangle\right) \tag{2.45}$$

$$\left|\phi^{\pm}\right\rangle = \frac{1}{\sqrt{2}} \left(|00\rangle \pm |11\rangle\right). \tag{2.46}$$

For simplicity, from now on we will omit the tensor product, that is, $|00\rangle = |0\rangle \otimes |0\rangle$. For the case of density operator there is $\mathcal{H}_{\mathcal{A}}$ and $\mathcal{H}_{\mathcal{B}}$ system respectively, and is represented by ρ^{AB}.

$$\rho^{AB} = \sum_{i=1}^{n} p_i \rho_i^A \otimes \rho_i^B \tag{2.47}$$

2.1.4 Quantum fidelity

Sometimes it is important to know how different two states are, for example state discrimination [10] or quantum tomography [23]. The quantum fidelity answer this question for some situations and quantify the distance between two states. Let ρ and ϱ two density operators and the fidelity of this two states is defined by

$$F(\rho, \varrho) = Tr\left(\sqrt{\sqrt{\rho}\varrho\sqrt{\rho}}\right)^2, \tag{2.48}$$

If ϱ is a pure state, the fidelity formula is reduced to

$$F(\rho, \varrho) = \langle\psi| \rho |\psi\rangle . \tag{2.49}$$

The parameter $F(\rho, \varrho) \in [0, 1]$, where 1 is maximum fidelity and represent that the both are the same state.

2.2 Quantum Information

In classical information theory can be use the classical bit, that represent the minimum unit for encode, decode and transmit information. Is the base for create the analogy in quantum information and formalize the minimum information, this is how it is built the quantum bit o qbit. In this subchapter we explain quantum bits, widely used in this thesis.

2.2.1 Quantum bits

The quantum bit is a element in a Hilbert space of two dimension. Are used as basis for describe protocols in quantum information like quantum cryptography [11], quantum teleportation [12] or experiment of twin photons entangled [20]. The mean different between the classical and quantum bits is that, meanwhile the classical bit have just two state (0 or 1), the quantum counterpart is a superposition between the state 0 and 1. The qubit with the Dirac notation is represent by

$$|\psi\rangle = \alpha |0\rangle + \beta |1\rangle \tag{2.50}$$

where α and β are the complex number and satisfy that $|\alpha|^2 + |\beta|^2 = 1$. The kets $|0\rangle$ and $|1\rangle$ former the computational basis and are orthogonal to each other ($\langle i|j\rangle = \delta_{ij}$). Other way of represent the qubit is function of angles, and the formula is

$$|\psi\rangle = e^{i\gamma}\left[cos\left(\frac{\theta}{2}\right)|0\rangle + e^{i\varphi}sin\left(\frac{\theta}{2}\right)|1\rangle\right], \tag{2.51}$$

where γ, θ and φ are the real numbers. The term $e^{i\gamma}$ is despised because is not physical observable. Now, how the equation (2.51) has two angles is possible represent in a tridimensional sphere, this is called *Bloch sphere*[9]

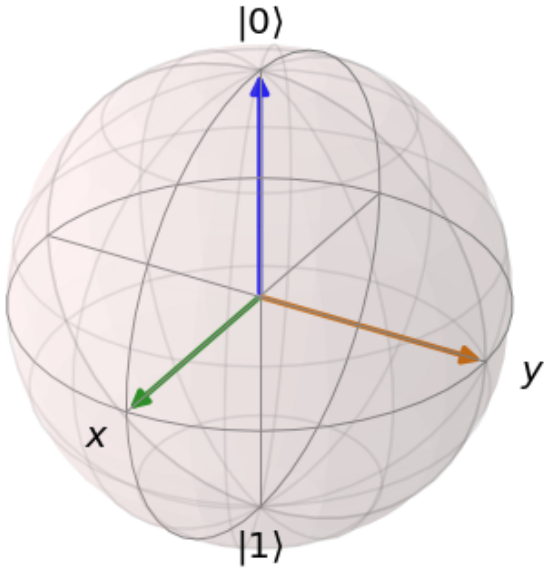

Figure 2.1: Is the graphical representation for the space of a qubit. In addition, the angle between orthogonal states is π. Source: Made by the author.

The angle θ and φ represent the spherical coordinate, so we can define the $\vec{r}$ vector

$$\vec{r} = (sin(\theta)cos(\phi), sin(\theta)sin(\phi), cos(\theta)) \tag{2.52}$$

where $\vec{r}$ is called Bloch vector, which has the components r_x, r_y and r_z. We can take this elements for represent a mixed state in function the identity matrix, Pauli matrices[10] and the aforementioned vector.

$$\rho = \frac{1}{2}(\mathbb{I} + \vec{r}\cdot\vec{\sigma}) \tag{2.53}$$

[9]Named after the Swiss-American physicist Felix Bloch, 1905-1983.
[10]Named after the Austrian physicist Wolfgang Pauli, 1900-1958

where the $\vec{\sigma}$ are the 2-dimensional Pauli matrices and are defined of the following form

$$\sigma_x = \begin{pmatrix} 0 & 1 \\ 1 & 0 \end{pmatrix}, \quad \sigma_y = \begin{pmatrix} 0 & -i \\ i & 0 \end{pmatrix}, \quad \sigma_z = \begin{pmatrix} 1 & 0 \\ 0 & -1 \end{pmatrix}, \tag{2.54}$$

If we expand the formula (2.53) using the the Pauli matrices, the density operator is explicity represented by

$$\begin{aligned} \rho &= \frac{1}{2}\begin{pmatrix} 1 & 0 \\ 0 & 1 \end{pmatrix} + \frac{r_x}{2}\begin{pmatrix} 0 & 1 \\ 1 & 0 \end{pmatrix} + \frac{r_y}{2}\begin{pmatrix} 0 & -i \\ i & 0 \end{pmatrix} + \frac{r_z}{2}\begin{pmatrix} 1 & 0 \\ 0 & -1 \end{pmatrix} \\ \rho &= \frac{1}{2}\begin{pmatrix} 1+r_x & r_x - ir_y \\ r_x + ir_y & 1 - r_z \end{pmatrix} \end{aligned} \tag{2.55}$$

The eigenvalues of the matrix (2.55) give the domain of $\vec{r}$.

$$det\left[\rho - \lambda \mathbb{I}\right] = 0 \tag{2.56}$$

$$(1-2\lambda)^2 - |\vec{r}|^2 = 0 \tag{2.57}$$

By the equation (2.57) we have the eigenvalues $\lambda_\pm = \frac{1}{2}(1 \pm |\vec{r}|)$. If replace in the purity parameter (see in the subchapter 2.1.4) we can recognize two case

$$Tr(\rho^2) = \lambda_-^2 + \lambda_+^2 = \frac{1}{2}(1 + |\vec{r}|^2) \tag{2.58}$$

where if the term $|\vec{r}| = 1$ is a pure state (shell of sphere) and is a mixed state if $|\vec{r}| \leq 1$ (inside of sphere).

Finally, for complete the qbits analysis we show the systems in high dimensions. If increase the dimension to a d-dimensional space instead of being called qbits they are quantum dits or qudits, and the can be represent for the following formula

$$|\psi\rangle = \sum_{i=0}^{d} c_i \, |i\rangle \tag{2.59}$$

where $\sum_{i=0}^{d} c_i^2 = 1$ and the kets $|i\rangle$ can be represent a canonical basis with more of two elements. For dimensions larger than 2 the qudits don't have graphical representation.

2.3 Spontaneous parametric down conversion

The previous section (2.1.3) showed how the entangled states are represented, in this chapter will detail how to produce entangled states like equations (2.45) and (2.46). The physical process to generate these types of states is framed within of no linear optics, this is, the relation between polarization density and electric field is quadratic or higher [25]. The process is called spontaneous parametric down conversion (SPDC), where two fields presented spatial and temporary correlations. The beginning of study started in 1969

with Krindach and Klyshko showing the properties of light in this process and realized experimentally for temporal correlation by Mandel group [15, 21] emerging here the name *twins photons*. The last correlation indicate that the photons were created at the same time.
SPDC star with a beam (pump) pumping a no linear crystal, so that the beam interacts with the crystal and generate two photons called idler and signal. the output fields are weakness and generally in infrared range. In all process there are the energy and momentum conservation, for which the relation of frequencies and wave vectors is given by

$$\begin{aligned} & Energy \\ E_p &= E_s + E_i \longrightarrow \hbar\omega_p = \hbar\omega_i + \hbar\omega_s \\ \omega_p &= \omega_i + \omega_s \longrightarrow \Delta\omega = 0 \end{aligned} \tag{2.60}$$

$$\begin{aligned} & Momentum \\ P_p &= P_s + E_i \longrightarrow \hbar k_p = \hbar k_i + \hbar k_s \\ k_p &= k_i + k_s \longrightarrow \Delta k = 0 \end{aligned} \tag{2.61}$$

The subscript p, i and s is for pump, idler and signal respectively. The equations (2.61) and (2.60) show the ideal case for generate twins photons and are called phase matching conditions. Sometimes, the output wave of SPDC depend of Δk and can be reduced the amplitude, so counter this effect the alternative is to use a medium with periodic nonlinearity. Such periodicity which adds a opposite phase and allow realign the the phases distributed. This called technique called quasi-phase matching (QPM) and new relation between wave vectors is

$$k_s + k_i + G = k_p \longrightarrow \Delta k = G \tag{2.62}$$

where G is a grid parameter and their relation with crystal is given by

$$G = \frac{m2\pi}{\Lambda} = mL_c \tag{2.63}$$

where Λ is one period in the crystal, L_c coherence length and m is the mth harmonic that can be decompose using the Fourier transform.

2.3.1 Quantum state of SPDC

The quantum state of SPDC process describe the signal-idler situation and can arise from classical description, followed of the electromagnetic field quantization. The first step is consider a no linear medium up to second order and a electric field $E(\vec{r}, t)$ propagating it. The system's Hamiltonian is given by

$$\mathcal{H}(t) = \mathcal{H}_0 + \mathcal{H}_I \tag{2.64}$$

where $\mathcal{H}_0$ is interact Hamiltonian of electric field and the first order linear component of the electric polarization. The term $\mathcal{H}_I$ contain the no linear interaction. the next is consider some considerations for avoid difficulties in the quantization of the field, it is that

between the environment and medium there are no electromagnetic boundaries. The birefringence can be consider classically, after the field is quantized. Is also consider that after the medium there are two interference filter, so the output spectrum of SPDC process is narrow.
Now in quantization procedure, we expand $E(\vec{r},t)$ in term of the plane waves

$$E(\vec{r},t) = E^{+}(\vec{r},t) + E^{-}(\vec{r},t). \tag{2.65}$$

From here on it continues withe usual quantization of fields, the is, the amplitudes are changed to quantum operator. Since now the Hamiltonian is operator, will be used for find the state $|\psi(t_0)\rangle$, where t_0 is time of interaction. The state at a t time is described by the operator evolution and the state in time t_0

$$|\psi(t)\rangle = \hat{U}(t)\,|\psi(0)\rangle\,, \tag{2.66}$$

where $\hat{U}$ is evolution operator

$$\hat{U} = exp\left(\frac{1}{i\hbar}\int_0^t \mathcal{H}^{'}(t^{'})dt\right) \tag{2.67}$$

After considerations and quantization, the spontaneous parametric down conversion state is presented

$$|\psi\rangle = |vac\rangle + \sum_{\sigma_s\sigma_i}\int d\omega_s \int d\omega_i \int dq_s \int dq_i \Phi_{\sigma_s\sigma_i}(q_s,q_i,\omega_s,\omega_i)\,|q_s,\omega s,\sigma_s\rangle\,|q_i,\omega_i,\sigma_i\rangle\,, \tag{2.68}$$

where $|q_j,\omega_j,\sigma_j\rangle$ is photon state (idler or signal) in a transverse component of the wave vector, the frequency ω_j and polarizations σ_j. The term Φ is function for describe the photons distribution and depend of susceptibility and the spectral function of filter consider in description. More details in appendix (A).

2.3.2 Type of SPDC

The SPDC state detailed in (2.68) has several advantages, the output photons show entanglement in transversal momentum, polarizations and frequency. These are same advantage that allow realize entanglement experiment [16, 17, 19, 18]. In this section show practical example with polarization as degree of freedom, and the classification for SPDC states. This kind of generations depend of polarization state of input and outputs. If we consider a particular case of the two output photons after the process with two polarization, called ordinary (o) and extraordinary (e) [26, 27], three cases emerge.

Type-0: This case the photons twins has the same polarization (ordinary or extraordinary) and matches with input polarizations

$$o_p \longrightarrow o_i + o_s \tag{2.69}$$

Type-I: For this type, the photons input is orthogonal to the output photons and idler and signal has the same polarizations

$$e_p \longleftrightarrow o_i + o_s \tag{2.70}$$

Type-II: The last types, the output photons are orthogonal polarizations and one photons matches with the photon input.

$$e_p \longleftrightarrow e_i + o_s \tag{2.71}$$

the nomenclature ordinary and extraordinary is just a label, idler or signal photon can be labeled with any of the two.

Considering the ordinary and extraordinary as polarizations of photons, we can take the types of generations for generate entanglement states. How the generations is classified, we can classify the no linear crystal (Crystal type 0, I and II). If joint two crystals type-0 or type-I, one in front of the other and pumped with diagonal or antidiagonal polarization the no linear crystal, can be generate a entanglement state in polarization. The details is generate a qubit $|D\rangle = 1/\sqrt{2}(|0\rangle + |1\rangle)$ or $|A\rangle = 1/\sqrt{2}(|0\rangle - |1\rangle)$ and place one crystal in 90^o with respect to the generation axis of the other crystal. Then, for example if the first crystal generate with $|H\rangle$ and the second crystal in $|V\rangle$. Then, two translated cones are generated by momentum of signal and idler and and adding path compensation elements (not rendered for simplicity), the indistinguishability is created in which crystal the pair of photons was generated. Show in Figure (2.3.2).

After that the one photon interact with the no linear crystal SPDC create two cones where one cone is only polarization $|H\rangle$ and the other is only polarization $|V\rangle$. The state is given by

$$|\psi\rangle \frac{1}{\sqrt{2}} \left(|H\rangle_s |H\rangle_i + |V\rangle_s |V\rangle_i\right) \tag{2.72}$$

where s and i is subscript for idler and signal. The other case that we can generate a entanglement state is with a crystal type-II. The pump beam can be polarization $|H\rangle$ or $|V\rangle$ and after the interaction the SPDC process generate two cones. Unlike the previous case, the cones generate the indistinguishably in two spots. The photon can be from top cone or lower cone. Details in Figure (2.3.2).
After the interaction, the output is a entangled state in polarization again of two photons and is given by

$$|\psi\rangle = \frac{1}{\sqrt{2}} \left(|H\rangle_s |V\rangle_i + |V\rangle_s |H\rangle_i\right) \tag{2.73}$$

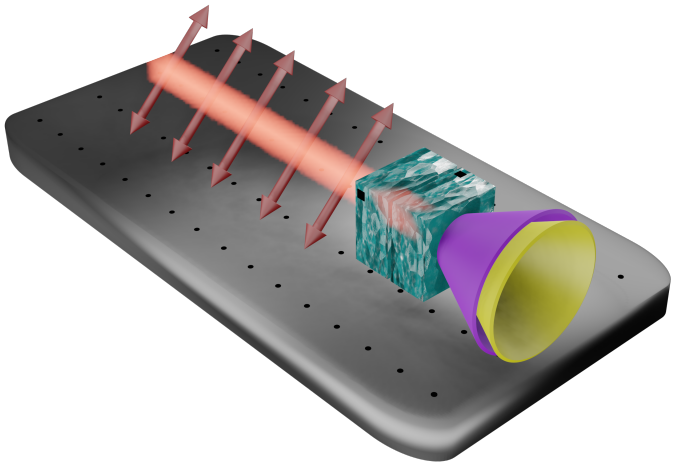

Figure 2.2: Generation of entangled state with two no linear crystals type I. The red light represent the pump and the arrows the diagonal polarization ($|D\rangle = \alpha |H\rangle + \beta |V\rangle$). The next are two no linear crystals type I, the second rotate in 90^o regarding the first where create the photons pairs. After, the two overlapping cones of signal and idler respectively (Yellow and purple). Source: Made by author.

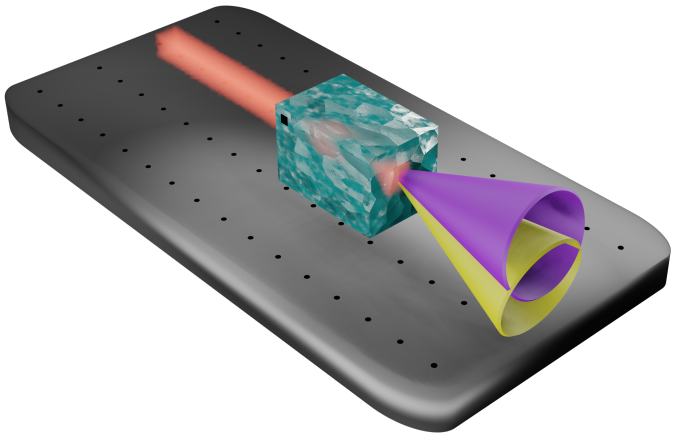

Figure 2.3: Generation of entangled state with no linear crystal type II. The red light represent the pump (Polarization is not plotted). The cube represents no linear crystal type-II. After, the two displaced cones that each have a different polarization. Where, the yellow and purple cone intersect generate the indistinguishably and create the entangled state. Source: Made by author.

It can be seen that the output state are equal to equations (2.45) and (2.46) and an experimental implementation can be seen in [95]. This mean that the letter inside the ket is just label and can represent other degree of freedom. In addition, like the bell state show maximal entanglement, that is, has the maximum entanglement in a quantum state.

2.4 Fiber optics

A powerful tool to transmit light without lens is a wave guide, they can come in various shapes and to confine the light have two refractive indices. This is the support to raise the idea of the optical fibers, a cylindrical dielectric waveguide with a refractive index n_1 in the center, called core and a refractive index n_2 on the edges, called cladding.

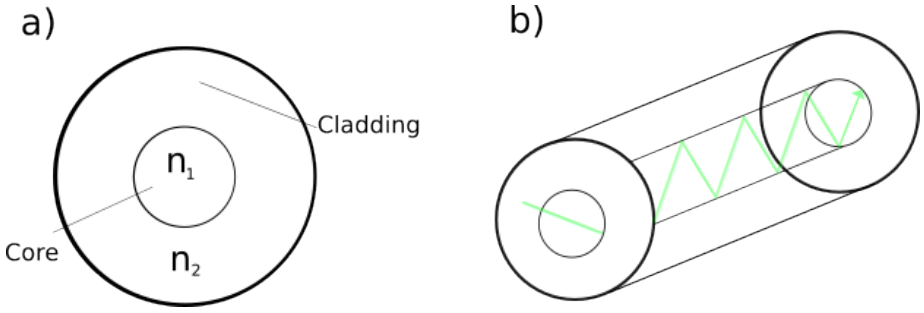

Figure 2.4: a) Front view of fiber where show the core and cladding with different refractive index. b) Side view showing the total internal reflection (green line) inside core fiber. Source: Made by the author.

The incident light travels through by the difference between n_1 and n_2[11], where $n_2 < n_1$. The trajectory of beam generates multiple reflections whit angle θ and $-\theta$ in each edge, accompanied by a phase shift of π in each reflection making 'total internal reflection'. In addition, the self-consistency is imposed, that is, if a wave plane travels after the reflections, it continue as wave plane [25].

There are two important classification for the fibers. the first type start with a fiber with diameter d that admits a beam of wavelength λ and their modes are defined by $M = 2d\lambda$, where if the $M = 1$ the fiber is called *single mode fiber* (SMF) and if $M > 1$ is called *multimode fiber* (MMF). The second classification is how the refractive index change inside the optical fiber. For the fibers with constant in core and a abrupt change when

[11]The difference between the refractive indices is 0.001 and 0.02

passing to the cladding are called Step-Index fibers, and if the refractive index change gradually is called graded-index fiber.

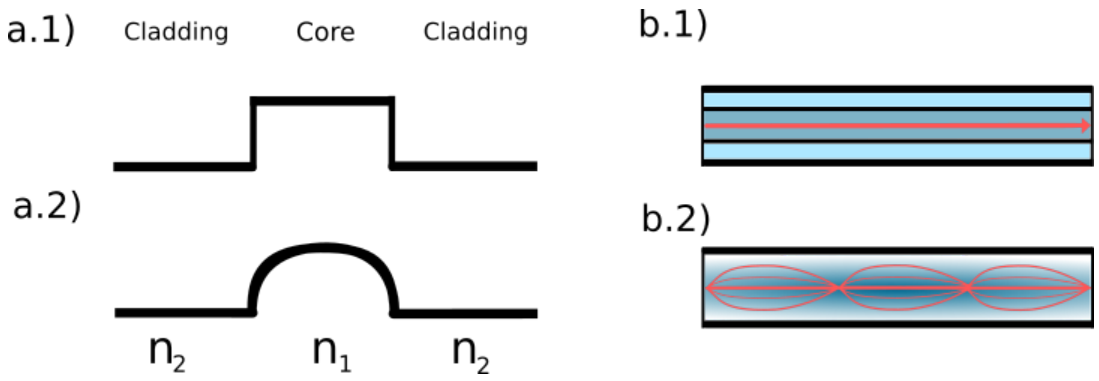

Figure 2.5: a.1) Step-index fiber with the radical change in the refractive index (black line). a.2) graded-index fiber with with a graduated exchange in the refractive index. b.1) Single mode fiber traveling in core's fiber (Dark blue). b.2) Multi mode fiber with graded refractive index. Source: Made by the author.

All these fibers is with one core, but the last case to analyze is when the fiber has more cores in the same cladding, called multicore fiber (MCF). This kind of fiber are fundamental tool in the these and and gives the initial kick to study multicore technology in the chapter (3), because allows multi channels of transmission in the same device. In this thesis we work with multicore fibers with four cores (Details in Figure 2.6).

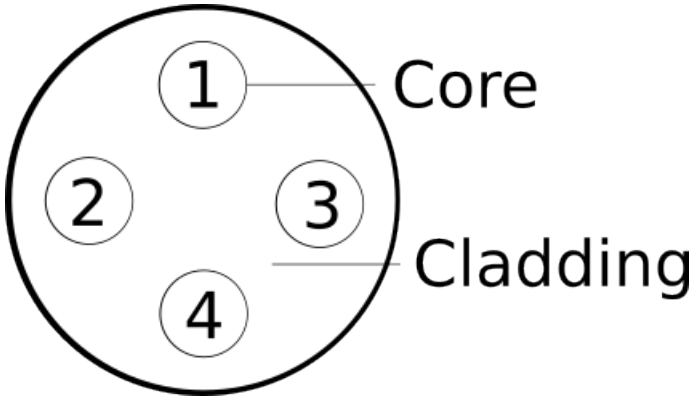

Figure 2.6: Front view of a multicore fiber with four cores in the same cladding. Source: Made by the author.

Chapter 3

Space-division multiplexing in quantum information

The fact of being able to guide the light using optical fibers (see in subchapter 2.4) undoubtedly opened a door to improve communications. That is because when the bits of information can be encoded on individual or entangled quantum states, an improvement is obtained over the traditional systems. For example, in security play an important role in QKD [11] protocols or quantum communication [31]. Then, the fiber optics and quantum states get together for the constant challenge expanding bandwidth [32]. For that, technology points towards to space-division multiplexing (SDM), and it consist of encoding the transversal spatial properties of light.
The union of these areas allows, on the one hand, to inquire about the degree of freedom in photonic [30] and take that knowledge to implement it in different type of optical fibers or optical components. Next we will show the details of types of fibers and other components that make up this area of SDM.

3.1 SDM in quantum information

Here, we show the devices used in the experimental setup, so we focus in two devices. The fibers and demultiplexers. An introduction for the fiber was mentioned in section (2.4), but it is necessary to elaborate on how they are used for SDM.
The fibers implemented for this experiment was in telecommunication band ($1200nm$ to $1600nm$), this allow you to have low losses ($< 0.2\ dB$ or $< 4.5\%$ per Km) and think that you can have good connectivity with other devices on de the same band. So, on the path for using these fibers and challenging the transmission capacity, a technique appears to using different wavelengths over single fiber, a technique is called wavelength division multiplexing (WDM) [34]. It is undoubtedly a good technique, but it is reaching its limits [32], so methods must be found to continue increasing transmission capacity. It is here where the aforementioned Space Division Multiplexing appears, which consists of exploring the different transversal modes of light and thus increasing the capacity.

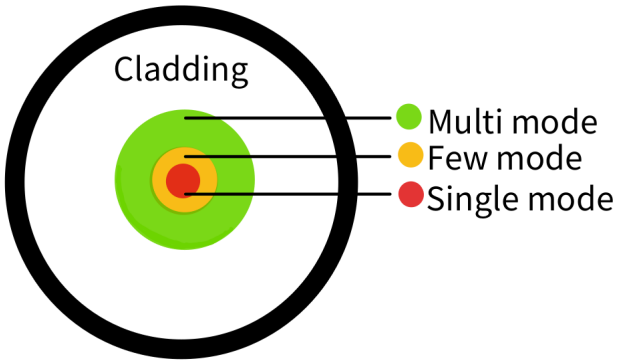

Figure 3.1: Front view of fiber core with different cores radios. Red: Outlines the core of a single mode fiber. Yellow: Outlines the core of a few mode fiber. Green: Outlines the core of a multimode fiber. Blank space represent the cladding of fiber. Source: Made by author

If the fiber support more than one mode, is suitable for SDM, but there are some considerations. A problem that you have when using multicore fibers is that light passes from one channel to another, damaging the encoded information, the so-called cross-talk. This is solved by keeping the distance between cores, specifically if the distance is more than $40\mu m$, we can consider each core as independent channel.
Some types of fibers were built prioritizing the numbers of cores [33], so the cross-talk problem returns but the solutions are the *trenches* or *holes*. Basically consist in change drastically the refractive index around the core (See details in Figure 3.2).
Another technique for use the fiber in SDM is based in that the core size influence the modes that it can admit. In the section 2.4 we mentioned that, if the fiber support one mode is single mode fiber and if support more than two mode is multi-mode fiber. The difference between admit one o more modes is directly related with core diameter (Figure 3.1), and we have one more case, when the fiber support some modes and using de parabolic refractive index (Figure 2.5-b.2), calls are created few-modes fibers [29]. With few mode reduce the detection complexity and we can mixed with multi-core fibers and thus implement several channel with few-mode fibers inside the same cladding (Figure 3.2).

The other device that we will review is the multiplexers and demultiplexers. Commonly called fan-in and fan-out respectively, this name is due to the characteristics of combine and split different channels of fiber. Each channel may be a SDM fiber.
The structures of these passive components[1] contain N independent single-mode input/output fibers, and are mapped onto a particular mode of an SDM fiber. From this type of device, some case arise such as photonic lanterns [35], that consist in input of single mode fibers and then are tapered together and finish in multi-mode fiber for other side. Other case is, if we include channels with different cores size, a mode selective lantern can be built [36]. For OAM-carrying optical modes, there are demultiplexers, called mode sorters [37], here have been using active elements. Furthermore, these device are a sample of low

[1]Passive components which require no input power to function. For example: Optics connectors, adapters, patch cords, etc.

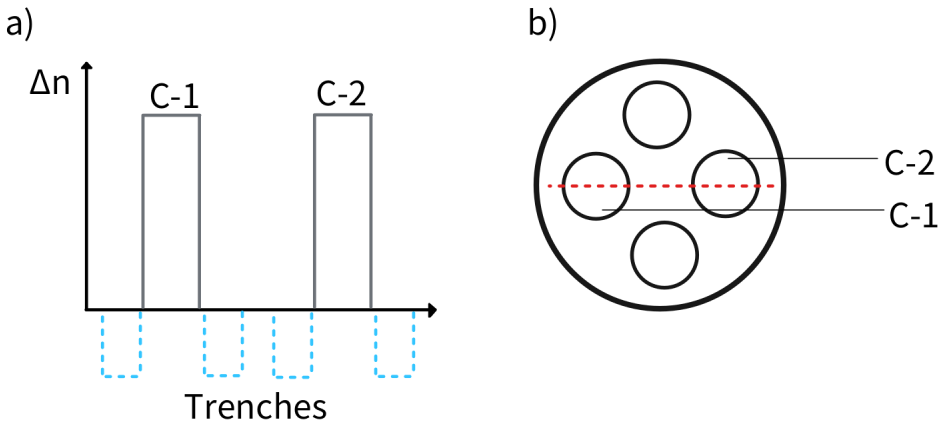

Figure 3.2: Cross-section schematics of SDM fiber. Source: Made by author. a) Relation between refractive index profile Δn and distance of core r. Light blue dotted lines represent the trenches and solid gray line the core 1 and 2. b) Front view of multicore fiber and dashed red line represent view of subplot *a*. Label $C-1$ and $C-2$ belong to cores 1 and 2 respectively. Source: Made by author.

losses with the technology used in this thesis, for example in demultiplexer with MCF with loss less than 0.35 and cross-talk less than $-64dB$ [38]. Then, the summary is that the multiplexers and demultiplexer is the connection between independent channel and *all in one* fiber (Figure B.1).

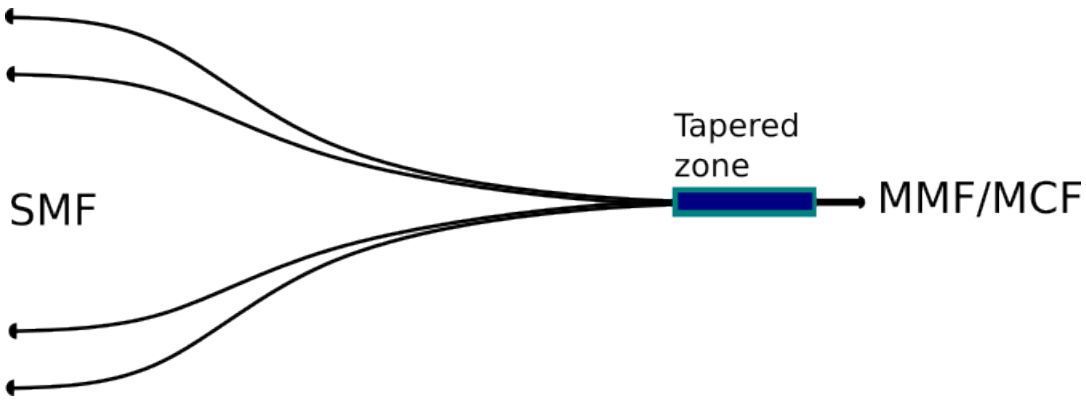

Figure 3.3: Schematic figure of Multiplexer/Demultiplexer. Left to right: Individual fibers that can be single mode fiber, the next is where the fibers are stretched to join into a single fiber. This passive device are bidirectional, the left fiber can be multi-mode or multi-core fiber. Source: Made by author.

3.2 Quantum states with SDM

I have already seen the basics of the devices that make up SDM, next I will show how these can be used with quantum information. These concepts point to areas used in this thesis, such as high dimenensional states, but also to the immediate future work, such as the applications that could be made in quantum information.

The first step is show that d-dimensional quantum state, called qudits and mentioned in section (2.2), are important and improve some task in quantum communications. For example in Bell inequalities, where prove several qu$N$its (definition used in the publication and it is analogous to qudits) in a inequality and the results show that at higher dimension the violation of local realism is better than for two qubits, in other words, the performance improve with higher N [39]. Other important realization of $d-$dimensional quantum state is ti encode information on the path, for example they used slit for generate maximally entangled state of $D-$dimensional (notation of publication) using the transverse spatial correlations. With a BBO crystal and manipulating the pump beam they achieve that the twin photons pass by slit only in the situation that they are symmetrically opposite [40]. Then, a $d-$dimensional path-encoded qudit has the general form

$$|\Psi\rangle = \frac{1}{\sqrt{C}} \sum_{d=0}^{d} e^{\phi_d} |d\rangle \tag{3.1}$$

where d represent the $d-$th path (can be slit, fiber, etc), ϕ_d is the relative phase in the path and C is the normalization constant. The previous equation shows that a path can be one dimension and is a direct advantage gained in quantum information when using $d-$dimensional states, because increase the transmission rate in protocol like QKD [41]. Furthermore, the more dimensions there is the possibility of encoding more bits by equation $log_2(d)$.

On the challenge side, which is the issue of implementing spatial HD-QKD. The problem with this is that it is difficult to preserve the phase at the wavefront of photons during propagation in the fibers. This topic is addressed in this thesis, but we use it in an uncontrolled way, showing the difficulty of manipulating the phases in the fibers.
Some experiments had been done, for example in [42] used hollow-core photonic crystal fiber[2] (HC-PCF) for distribution of quantum entanglement, but intermodal dispersion and intermodal mixing produce decoherence of quantum superposition during propagation. The appearance of the SDM fibers changes the paradigm, since this kind of fibers support many modes at a less cost. A example of this is research is [43], is a experimental setup of a 300 meters of multicore fiber and is used for implement a HD-QKD with deformable mirrors as the phase modulators, the improved the results of the spatial light modulators (SLM).

[2]Hollow core fiber is formed by silica glass membranes with shape of cells and in the center of fiber is create a *hollow* removing some unit of cells.

Chapter 4

Qubits entanglement source

Once the theoretical bases have been shown, the experimental part of this work is shown. Contains this chapter and the next, the following being the main one of the thesis. However, It's important what the transit was, experimentally speaking, to reach a multi-dimensional source.

The first subchapter is based on the work published in 2019 [20] and is a polarization entanglement source, that generate partially entanglement states (PES). The performance of these states with different degree of entanglement was tested in Self-testing and Randomness generation in a device-independent scenario (DI).
The second work, which is based on the publication made in 2021 [47] and used the fact that in the states with the lowest entanglement it was not possible to overcome the nonlocal limit. An optimization is performed over the same statistics and see if new parameters can overcome the result obtained in [20].

4.1 Experimental investigation of PES for D-I randomness generation and self-testing

The first experimental setup, was a polarization entanglement source based on Sagnac interferometer and nonlinar crystal, more details in Figure 4.1. The PPLN-II crystal is pumped with a continuous wave laser at 405 nm in diagonal polarization. The beam is split in Dual PBS, causing[1] the crystal generate SPDC process through both paths of the interferometer. The photons pairs generated recombine in Dual PBS, after Alice and Bob will receive photons in both orthogonal polarizations. This served to create

[1]It should be mentioned that this is achieved because in the reflected path there is an HWP_s set at 45^o with respect to the horizontal axis.

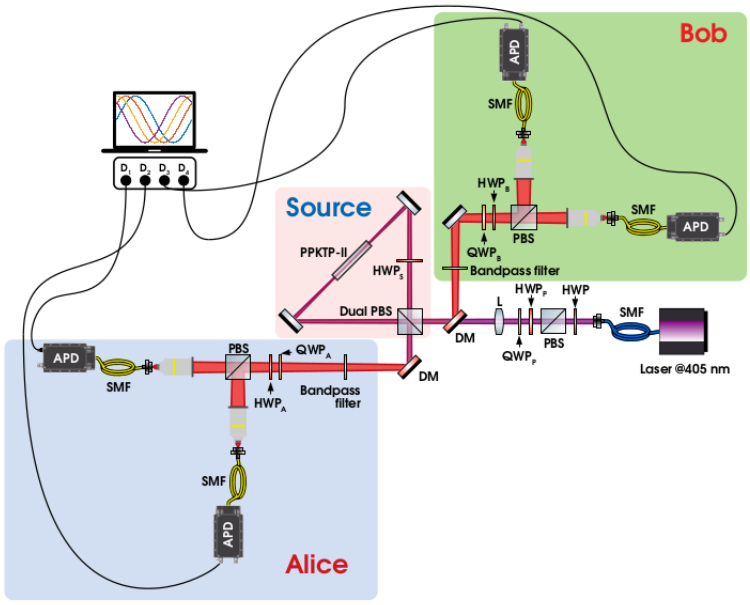

Figure 4.1: Experimental setup used for randomness certification and self-testing. Source: reprinted with permission from [20].

indistinguishably in the degree of freedom of photon polarization and resulting a entangled polarized state

$$|\Psi\rangle = \alpha\,|H\rangle_i\,|V\rangle_s + \beta\,|V\rangle_i\,|H\rangle_s \tag{4.1}$$

where $|H\rangle_i\,|V\rangle_s = |H\rangle_i \otimes |V\rangle_s$, the index i and j are from idler and signal respectively. In addition, the coefficients α and β are from linear superposition of the polarization of pump $\beta\,|H\rangle + \alpha\,|V\rangle$. This feature of the source, of being able to change the polarization allow us to unbalance the power on the path of the interferometer and as a consequence change the generation in the crystal, which ends up changing the degree of entanglement of state. In the case of our experiment, five partially entangled states (PES) were generated and were chosen to cover the entire range of concurrence (0.2, 0.4, 0.6, 0.8 and 1, where the 0 is separable state and 1 is maximally entangled state).

4.1.1 Self-testing and Randomness certification

All these states were tested in a real scenario to carry out two protocols, the randomness generation and self-testing. To the certify the protocols, non-locality had to be verified, so measurements were made to see if the system violated a Bell's inequality, which was specially chosen for study two entangled qubits. The first step was a quantum tomography all state ρ_t reconstructed present degrees of purity $Tr\left[\rho_t^2\right]$ above 0.985. We also calculate the degree of entanglement of ρ_t as measured by the concurrence. We then proceed to find the closest pure PES, $|\Psi(\theta)\rangle$, by maximizing the fidelity

$$F\left(\rho_t, |\Psi(\theta)\rangle\,\langle\Psi(\theta)|\right) = \langle\Psi(\theta)|\,\rho_t\,|\Psi(\theta)\rangle \tag{4.2}$$

This allows to estimate the fidelity with the target PES and the corresponding angle θ. Details in Figure 4.2.

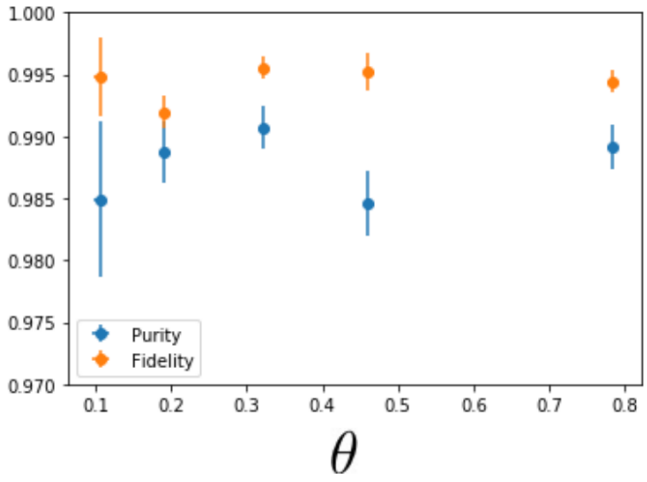

Figure 4.2: Purity (Blue points) and the fidelity (orange points) with respect to the closest PES obtained from quantum tomography. Source: reprinted with permission from [20].

Another point to highlight is that all the reconstructed states show a remarkably high fidelities with pure PESs of the form of $|\Psi(\theta)\rangle$, all of the being larger than 0.99.
As a result of the tomography, we obtain the θ angle, the we allow choose the setting an pure Bell experiment and set $\alpha = 2/\sqrt{1+2tan^2(2\theta)}$ parameter of the inequality. The tilted inequality used was introduced in [44] to study properties of pure two-qubit entangled states. Is given by

$$B_\alpha = \alpha\langle A_0\rangle + \sum_{j,k=0}^{1}(-1)^{jk}\langle A_j \times B_k\rangle \leq \alpha + 2 \tag{4.3}$$

The expectation values are a function of the conditional probabilities and $0 \leq \alpha \leq 2$. Its maximal quantum violation is equal to $B_\alpha^{max} = \sqrt{8+2\alpha^2}$ and can be obtained by performing appropriate measurements on the states

$$|\Psi(\theta)\rangle = cos(\theta)\,|00\rangle + sin(\theta)\,|11\rangle \tag{4.4}$$

The results obtained in inequality showed that the more entanglement the state was, the grater the gap between the local bound and maximal violation of Bell's inequality (See figure 4.3).

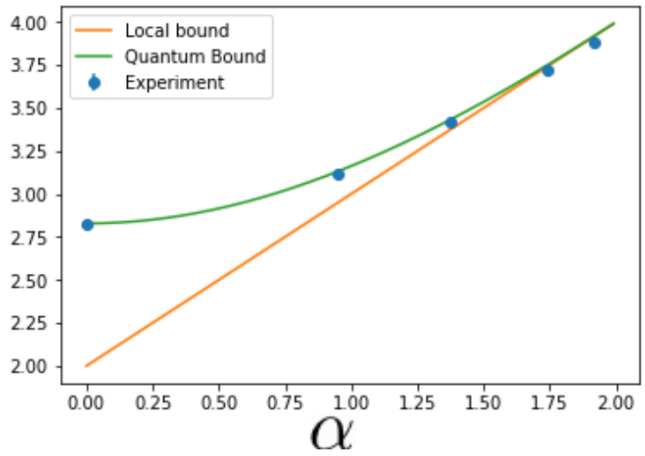

Figure 4.3: Observed violation of the tilted Bell inequality. The orange line corresponds to the local bound, above which non-locality can be proven. The green line is the maximal violation that can be achieved, while the blue dots are the experimental values obtained. Source: reprinted with permission from [20].

For Randomness certification we need make statistics non-local, that is why it is required that the Bell's inequality be violated. It also ensure that the outcomes can be predicted [51]. This unpredictability can be estimated by assuming the worst-case scenario where the two quantum particles in devices A and B are correlated with a third quantum particle held by an eavesdropper Eve, the global tripartite being pure and denoted by $|\Psi\rangle$. Eve's goal is to guess the output a for a particular measurement choice x^* by performing a measurement on her part of the state. Eve is assumed to know $|\Psi\rangle$ and the measurements implemented by boxes A and B. he randomness of a when $x = x^*$ can be estimated through the guessing probability [45, 46]

$$P_{guess} = max \sum \langle\Psi| \prod_{a|x} \otimes \mathbb{I} \otimes \prod_{e=a} |\Psi\rangle \tag{4.5}$$

This quantity gives the maximum probability that Eve's outcome e matches the user's outcome a for measurement x^* over all possible quantum realizations. The estimated randomness can be expressed in bits by $R = -log_2(P_{guess})$.
We compare the equation (4.5) with the concurrence computed through quantum tomography. The performance of the five PES in the Randomness certification in the Figure (4.4).

For second protocol, self-testing, used the fidelity between ρ state of A-B system and and the state to be self tested (4.4). The fidelity formula is give by

$$\max_{\Lambda_A,\, \Lambda_B} \; F((\Lambda_A \otimes \Lambda_B)\rho, |\psi(\theta)\rangle \langle\psi(\theta)|) \geq s_\alpha \cdot B_\alpha + \mu_\alpha, \tag{4.6}$$

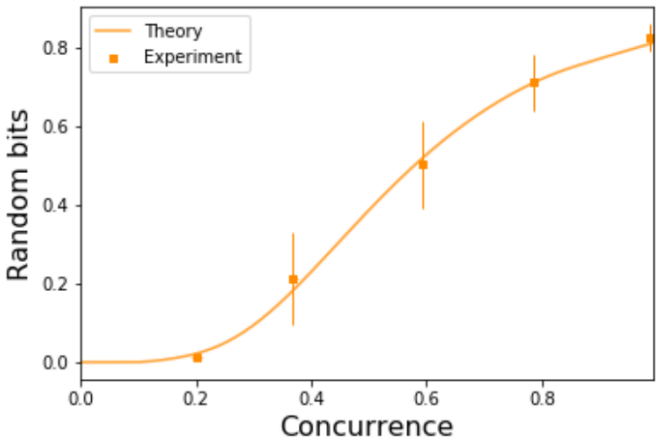

Figure 4.4: Experimental randomness certification as a function of entanglement. Almost all the cases can certify randomness. However, they are far from, in principle, the possible value of 1 bit of randomness. Source: reprinted with permission from [20].

The previous equation was calculated only with expectation values involved in the violation of the tilted Bell inequality. In our experiment, those probabilities were computed for those settings chosen from the estimation of the angle θ. The optimal α parameter is α^* and we get after optimize equation (4.6) and the optimal θ^* results. The behavior of all state in the self-testing protocol can be seen in the Figure (4.5).

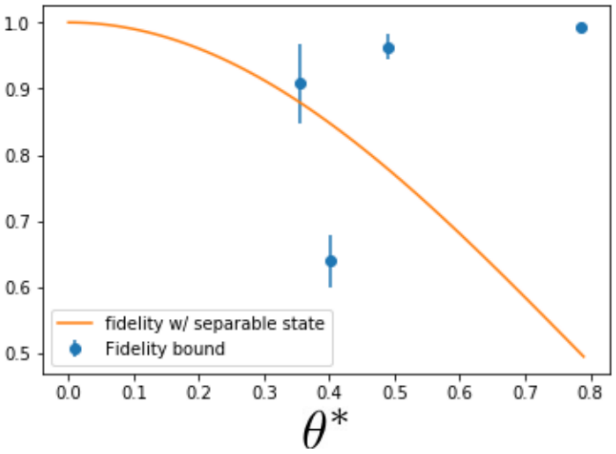

Figure 4.5: Fidelity bounds with respect to target PES. The solid orange line, added as a reference, shows the fidelity of a partially entangled state and a fully separable ones. In the horizontal axis the angle θ that is self-tested by the fidelity bound.

In conclusion, a marked trend can be seen in the Figures (4.2), (4.4) and (4.5), and the more the entanglement of the PESs sates, the performance is better. Now, the states decay quickly despite the low noise level. It can even be seen that the two states with low degree of entanglement do not exceed the local limit in Bell inequality. Summary of all

parameter in table (4.1).

Theoretical concurrence	0.2	0.4	0.6	0.8	1
Experimental concurrence	0.1926	0.3746	0.5825	0.8349	0.9858
Purity	0.9849	0.9887	0.9907	0.9846	0.9891
α	1.914	1.741	1.373	0.949	0.0017
$B_\alpha \pm 0.01$	3.88	3.72	3.41	3.11	2.81
$\frac{B_{\alpha-L}}{Q-L}$	-32.84	-2.14	0.78	0.91	0.98
Angle θ	0.10539	0.19002	0.32140	0.45946	0.7847
Angle θ^*	NA	0.40059	0.35369	0.48907	0.78536
ϵ	0.0101	0.0143	0.0110	0.0111	0.0126

Table 4.1: Summary of experimental results.

4.2 Optimal strategy to certify quantum nonlocality

From Table 4.1, you can see how challenging it was to generate the states with concurrency 0.2 and 0.4. In specific, show that these two state failed by not exceeding the local limit. Then, a strategy was sought to improve the result but without needing new measurements. This was what was answered in [47] and it was the following work that was carried out with the results obtained from the entanglement source. Then, the objective was to show that with the same statistic that did previously failed, non-locality could now be certified after an optimization. In specific, is increase the gap between local hidden variable (LHV) and quantum results, achieved a better result in all PES states (see Figure 4.6).

Certification of quantum nonlocality becomes difficult in certain situations such as weakly entanglement or when the source of error is high. Here, a technique is proposed to find a Bell inequality with the largest possible gap between the quantum prediction and the local hidden variable limit for a given set of measurement frequencies. In method used certify the nonlocality from same statistics and does not require additional measurements. As shown in [48], in bipartite scenario it is possible to achieve a large quantum over LHV values ratios, equal to $\sqrt{n}/log(n)$, for n settings and n outputs in n dimensional Hilbert space. However, when testing quantum nonlocality, one is particularly interested in a state and measurements that maximize the violation of a given Bell inequality. From the experimental perspective, a larger theoretical violation increases the chance to certify quantum nonlocality in the laboratory. Nonetheless, sometimes experiments are not conclusive to certify nonlocality. When failing to test nonlocality in the laboratory, one can choose another Bell inequality with a larger gap between the LHV and quantum values, thus increasing the chances to success. However, the cost of this option is to implement a new experiment, as the optimal settings of the new Bell inequality most likely differ from the original one. This procedure consumes additional time and resources.

Thus, a fundamental question arises: *Can we certify quantum nonlocality from experimental data that failed to violate a target Bell inequality?* In this work, we find necessary and sufficient conditions to provide a conclusive answer to this question, for any bipartite scenario.

The method consist in increasing the gap between quantum and LHV prediction, i.e improve the chances that the same statistic can surpass the LHV and be non-local. This stars with a Bell inequality for a bipartite scenario [49]:

$$\sum_{x,y=0}^{m-1}\sum_{a,b=0}^{d-1} s_{xy}^{ab}\, p(a,b|x,y) \leq \mathcal{C}(s), \tag{4.7}$$

where $p(a,b|x,y)$ is the probability of obtaining outcomes $a,b \in \{0,\ldots,d-1\}$ when inputs $x,y \in \{0,\ldots,m-1\}$ are chosen by two observers Alice and Bob, respectively. Besides, $\mathcal{C}$ is the local values and if this bound is violated, a quantum system is present. Without loss of generality, we can restrict out attention to parameters within the set $-1 \leq s_{xy}^{ab} \leq 1$, for every $a,b = 0,\ldots,d-1$ and $x,y = 0,\ldots,m-1$.
Quantum joint probability distributions satisfy the no-signaling principle. In particular, the outcome of one party cannot reveal information about the input of the other. That is,

$$\sum_{b=0}^{d-1} p(a,b|x,y) = \sum_{b=0}^{d-1} p(a,b|x,y') =: p_A(a|x), \tag{4.8}$$

and

$$\sum_{a=0}^{d-1} p(a,b|x,y) = \sum_{a=0}^{d-1} p(a,b|x',y) =: p_B(b|y), \tag{4.9}$$

for every $x \neq x'$ and $y \neq y'$, where $p_A(a|x)$ and $p_B(b|y)$ are the marginal probability distributions associated to Alice and Bob, respectively.

Let us now consider a set of relative frequencies $f(a,b|x,y)$ of occurrence for outcomes a,b when x,y is measured by Alice and Bob, respectively, obtained from experimental data. The no-signaling constraints (4.8) and (4.9) do not occur due to errors but they can be recovered by minimizing the Kullback-Leible divergence [50]:

$$D_{KL}(\vec{f}||\vec{P}) = \sum_{a,b,x,y} f(x,y) f(a,b|x,y) \log_2 \left[\frac{f(a,b|x,y)}{P(a,b|x,y)}\right], \tag{4.10}$$

where $f(x,y)$ is the relative frequency of implementing a measurement x by Alice and y by Bob, and $p(a,b|x,y)$ the optimization variables, consisting of a joint probability distribution within the framework of quantum mechanics. The minimization procedure (4.10) is equivalent to maximize the likelihood of producing the observed frequency $p(a,b|x,y)$, see Appendix D1 in [50].

The experimental prediction of a Bell inequality (4.7) defined by coefficients s_{xy}^{ab} is given by

$$\mathcal{Q} = \sum_{x,y=0}^{m-1}\sum_{a,b=0}^{d-1} s_{xy}^{ab}\, p(a,b|x,y), \tag{4.11}$$

having associated an error propagation $\Delta\mathcal{Q}$. An experimentally obtained probability distribution $p(a,b|x,y)$, associated to errors $\Delta p(a,b|x,y)$, is certainty nonlocal if $\mathcal{Q}-\mathcal{C} > \Delta\mathcal{Q}$, for a given Bell inequality. However, sometimes quantum nonlocality cannot be reveal due to the amount of errors, especially when a weakly entangled quantum state produces the maximal violation of the inequality. Under such situation, the method introduced provides a new Bell inequality that increases the chances to prove quantum nonlocality for a given set of probability distributions $p(a,b|x,y)$, associated to experimental errors $\Delta p(a,b|x,y)$. The method consists in solving the following nonlinear problem:

$$R = \max_{s} \frac{\mathcal{Q}(s) - \Delta\mathcal{Q}(s) + dm}{\mathcal{C}(s) + dm}, \tag{4.12}$$

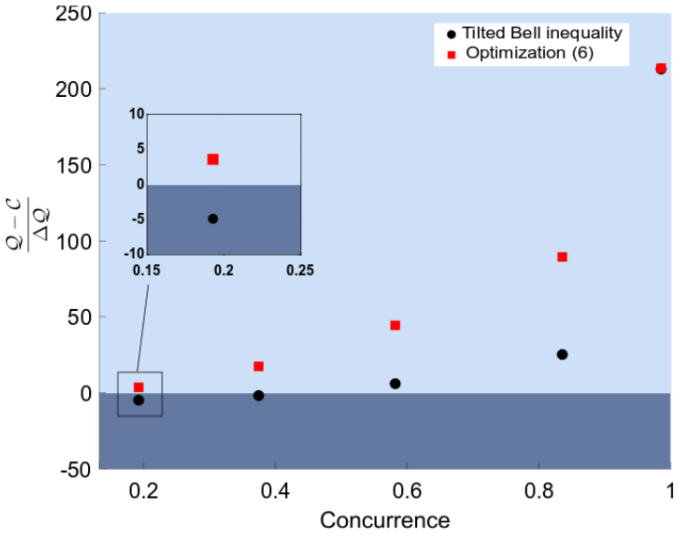

Figure 4.6: The standard deviation number (SDN) as a function of concurrence. For each value of concurrence, the optimization procedure (4.12) provides a Bell inequality that increases the number of standard deviations of the quantum-LHV value gap. SDN is calculated for two cases: tilted Bell inequality [black circles] and inequality arising from optimization (4.12) [red squares]. In both cases, we consider experimental data, where quantum nonlocality can be certified in the light blue region. For concurrences $C = 0.375$ and $C = 0.193$, there is no quantum violation of the tilted Bell inequality, whereas inequalities arising from optimization (4.12) produce a violation in all the cases.

When nonlocality certification from a given set of experimental data fails our method provides a "second chance" to do it, without requiring to perform any additional measurement.

Here, we considerably increased some previously obtained gaps, fact that allowed us to certify nonlocality for low values of concurrences, something that was not possible to do with the tilted Bell inequality.

Chapter 5

High dimensional state with optical fibers

In the previous sections, the concepts of qudits (section 2.2.1) and spatial division multiplexing (section 3.1) were defined, but now we will put these concepts together and they will be shown how they were brought to the experimental level, to then characterize the source and quantify the entanglement.
In quantum information, there are several protocols that its performance is better when using the quantum states of d-dimensional (qudits). For instance, single qudits states can be exploited for building quantum cryptographic schemes supporting solving component imperfections [52], for efficient strategies solving communication complexity problems [53, 54] and for advanced phase-estimation algorithms [55, 56]. Specifically, some Bell inequalities for qudits have the property that their genuine quantum violation can still be achieved while working with lower (compared to qubits) overall detection efficiencies [57], which is arguably the main technological challenge of loophole-free Bell experiments. Second, there is a family of Bell inequalities specially tailored for entangled qudits [58, 59], whose quantum violation can still be achieved in a regime where noisy setups would be regarded as useless if based solely on the famous Clauser-Horne-Shimony-Holt Bell inequality [60, 61].

Traditionally, the transverse momentum of single photons has been used for encoding qudit states for over almost two decades now [62, 63, 40]. The distribution of photonic quantum states using optical fibers is a fundamental building block towards quantum networks, but due to effects such as decoherence-inducing mode coupling and limited amount of modes supported, the transmission of such spatially encoded qudits over conventional multi-mode and single-mode fibers has always been considered a formidable challenge. Interesting strategies in this direction have been presented recently [64, 65], but they are still limited to the transmission in the range of a few meters for multi-mode fibers, and unable to fully exploit the advantages provided by qudits in the case of single-mode fibers (SMF). Alternatively, there is a new trend emerging for the fiber propagation of spatially encoded qudits that is based on new types of optical fibers developed for space-division multiplexing (SDM) in classical telecommunications [66]. Basically, SDM technology increases data transmission in classical networks by adopting fibers capable of simultaneously supporting

several transverse optical modes, where the information is then multiplexed [32]. Since mode coupling in these fibers is minimal, high-fidelity coherent transmission of entangled and single spatially encoded qudits has been already demonstrated up to a few kilometers [67, 68, 70].

In this work we introduce a new source of entangled path-encoded qudit states, which is fully based on SDM multi-core fiber (MCF) technology. Multi-core fibers have several cores within the same cladding, and each core mode can be used to define the logical basis in the path encoding strategy, as we explain below. Moreover, the relative phase between two different cores of a MCF has been shown to be orders of magnitude more stable than two single-mode fibers [70]. Consequently, these fibers have already been exploited for multi-dimensional quantum cryptography [43, 71], quantum random number generation [72], quantum computation [56], and Bell inequality violation [73, 74]. Path encoding has the important appealing that d-dimensional arbitrary operations can be implemented with conventional linear optical elements [75], and has now become the standard encoding strategy in experiments with integrated photonic circuits [76, 77]. Therefore, our source of path entanglement can be used as a resource for the implementation of entanglement-based quantum information protocols in experiments based solely on new MCF technology [72], or also to efficiently distribute multi-dimensional entanglement between integrated circuits, which are proven to be compatible with MCFs [71]. Our source compares favorably in terms of integrability and brightness with previous works for fiber-based generation of multi-dimensional path entanglement [73, 74, 78], and represents an important step towards the compatibility of quantum communications with the next-generation SDM optical networks.

5.1 Quantum information with MCF technology

Multi-core fiber is currently being pursued for its capability to increase communications rates in telecommunications [32]. At the same time, several authors have investigated MCF technologies in photonic quantum information platforms (Complete review in [66]). Here we employ four-core fibers (4CFs henceforth). Figure (5.1) a) shows an image of the facet of a 4CF taken with a standard fiber-inspection microscope and a camera. The cores are $\sim 8\mu m$ wide, corresponding to single-mode at $1550\mu m$, arranged on the vertices of a square with $50\mu m$ sides, which is large enough so that cross-core coupling is greatly reduced. This allows us to treat the spatial modes of each core as independent. For the 4CF, we thus define the path logical basis consisting of the core states $|j\rangle$ $(j = 0, ..., 0)$ as also shown in Figure (5.1-a) .
In addition to patchcords of MCF, crucial MCF-compatible optical devices have been recently developed that will allow widespread use of MCF technology in photonic quantum information. First is the demultiplexer (DM) device, as exemplified in Figure (5.1-b), which allows one to couple N single-mode fibers to an N-core fiber. With this, light can be sent from a standard single-mode fiber into one core of a MCF or vice versa, providing compatibility with standard optical fiber components. For example, we can couple a photon

in mode $|j\rangle$ of an MCF via a DM to a fiber-ready single-photon detector.

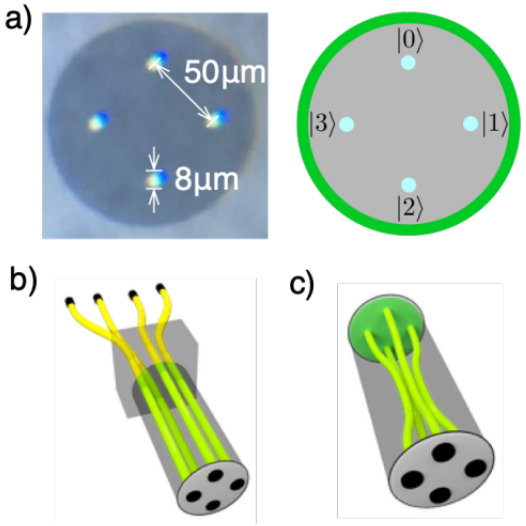

Figure 5.1: a) Photo of a multi-core fiber with four cores (4CF) taken with a camera and a fiber microscope (left), and diagram of the path-encoding strategy for defining the logical states in dimension d = 4 (right). b) The demultiplexer device, coupling single-mode fibers to a multi-core fiber (here 4CF). c) A 4×4 beam splitter constructed within a 4CF.

Another important device is the MCF-based beam splitter (MCF-BS), shown in Figure (5.1-c) or a 4CF. The beam splitter is produced by heating and stretching a section of homogeneous MCF (without refractive index trenches), so that the the cores become closer together, enabling evanescent coupling between the cores [79]. The 4CF-BS and a 7CF-BS were characterized experimentally in Reference [72]. When the proximity region is small, one can achieve an approximate 25% coupling between all four cores of a 4CF [72]. In the experiment reported here, we use two types of 4CF-BS devices. The first has been designed for use at $775nm$, and the second at $1550nm$. More technical details are given below. To reasonable approximation, the 4CF-BS can be represented by the unitary matrix

$$U_{BS} = \frac{1}{2}\begin{pmatrix} 1 & 1 & 1 & 1 \\ 1 & 1 & -1 & -1 \\ 1 & -1 & 1 & -1 \\ 1 & -1 & -1 & 1 \end{pmatrix} \tag{5.1}$$

The 4CF-BS thus takes a photon in path state $|j\rangle$ to an equally-weighted superposition state of the form $|\psi_j\rangle = \frac{1}{2}\sum_k u_{kj}\,|k\rangle$, where $u_{kj} = \pm 1$ are the entries of the matrix (5.1). Likewise, the 4CF-BS can be used to map superposition states into logical basis states: $U_{BS}\,|\psi_j\rangle = |j\rangle$.
These MCF devices can be connected with relatively low losses (about 2-5% at 1550 nm) using standard FC/PC fiber connectors [72]. We note that the future development of one

more MCF-based optical primitive, namely MCF-integrated phase shifters, will allow for entire multi-path optical circuits to be created entirely within multi-core fibers. This will allow for implementation of complex interferometers in a relatively stable MCF platform [70], for use in both quantum and classical optics applications such as communications and metrology. Moreover, multi-port beam splitter devices have recently been shown to provide advantages in quantum logic operations [80, 81]. This motivates the development of entangled-photon sources that are compatible with MCF technology.

5.2 Experiment

5.2.1 Setup

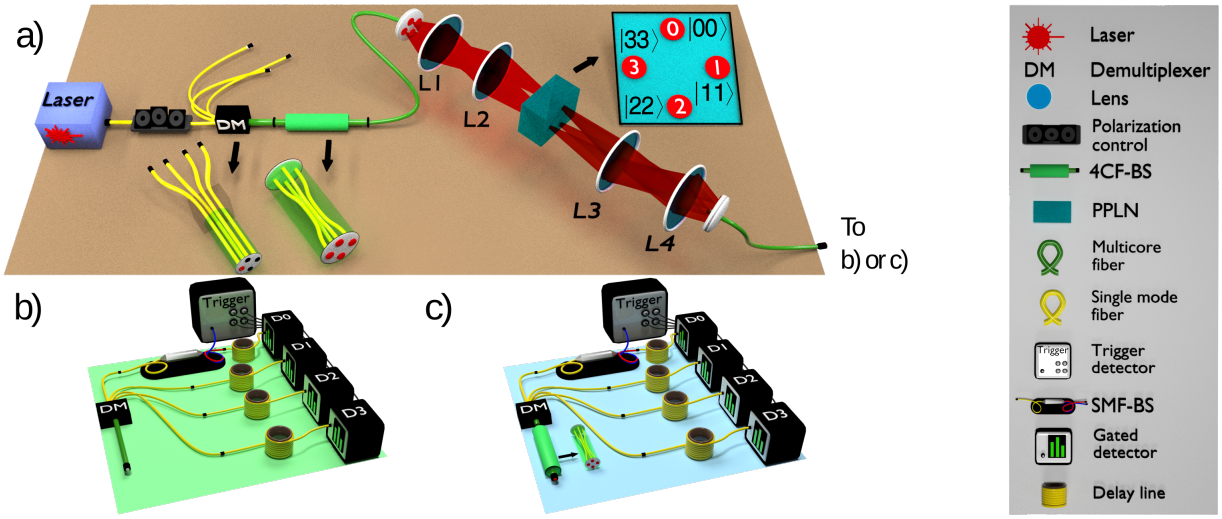

Figure 5.2: Experimental setup. The entangled qudits source generated by SPDC process in the PPLN non-linear crystal and SDM devices. The source are split in three stages. a) The preparation stage where we using laser, demultiplexer, Beam splitter multicore (4CF-BS), optics system and multicore fibres (MCF). b) First measurement stage: Detection system for Z measurement, in which each core of the source output MCF is coupled to a SMF via demultiplexer DM. c) Second measurement stage: Detection system for X_j basis and is the same structure that previous stage, but the 4CF-BS is added. Source: Made by author.

Here the cornerstone of this work will be explained, a experimental setup of Spontaneous parametric down conversion source for generate correlated photon pairs [82, 83]. The entanglement is based in indistinguishably of paths and use the SPDC process for built a qudit quantum state, which used the ste-of-art MCF technology (See details in Figure 5.2.1). The experimental setup stars with a continuous wave diode laser at 773 nm and is

used to pump the nonlinear crystal periodically poled lithium niobate (PPLN) type-0 of 1 cm, this create the down-converted photon pairs at a center wavelength of 1546 nm. One goal was that the source should be scalable, to have high spectral brightness and stable performance. The main idea is coherently illuminate the PPLN crystal in $n - regions$, where the n is the cores numbers of MCF and our case was four (Same shape of the Figure 2.6). The multi-spot coherent illumination of non-linear crystals for the generation of path-entangled photons was first presented in the 1990's [84] and has been used frequently since then [74, 77, 78]. However, this work points towards to the connectivity and compactness with the next-generation optical fiber networks. To coherently illuminate our PPLN crystal in a robust and efficient way, we take advantage of the developed MCF beam splitters described above [72]. The pump laser was connected to a SMF of the DM, and consequently coupled to a single core of the 4CF at its output side. Then, the pump beam is sent through a custom made 4CF-BS, designed to operate at $775nm$, that coherently splits the pump beam among the four cores of the 4CF. The first and complete split ratios characterization in appendix (B) and recorder for our experiment is 23.79%, 24.88, 27.19 and 24.14% at 773 nm. A fiber polarization controller (PC), placed before the DM, was used to guarantee that the pump polarization could be aligned with the extraordinary axis of the PPLN crystal, to maximize the photon pair generation rate.

The output face of the 4CF-BS was imaged using the $2f-2f'$ imaging configuration onto a plane at the center of the PPLN crystal using lenses L_1 (focal length $f = 11mm$) and L_2 ($f' = 50nm$), arranged confocally, giving a $\sim 4.5\times$ magnified image of the 4CF face. The down-converted pairs are produced at each one of the illuminated regions corresponding to the four fiber cores of the MCF (See the crystal inset of Figure 5.2.1). The generated photon pairs are then sent through confocal lenses L_3 ($f = 50\ mm$) and L_4 ($f = 11\ mm$) that perform the inverse operation: creating a de-magnified image of the down-converted pairs at the face of the output 4CF, coupling them into the fiber. The details of how the magnification factor was found in appendix (C.1) and (C.2). A bandpass and interference filter centered at 1550 nm are used (between the lenses, not shown for sake of clarity) to remove the remaining light from the pump beam.
Considering the split ratio recorded of the 4CF-BS, and that it is not possible in principle to distinguish which region of the crystal produced the photon pair, the generated two-photon state can be approximately written as a coherent superposition of the form

$$|\Psi\rangle = \frac{1}{2}\left(|00\rangle + |11\rangle + |22\rangle + |33\rangle\right) \tag{5.2}$$

Generated the photons, they couple to the output MCF after optical system and are sent to one of two measurement scenario, Figure 5.2.1 b) and 5.2.1 c). In each of these, photon pairs were detected by measuring coincidence counts C_{jk} $(j, k = 0, 1, 2, 3)$, where here j and k refer to the core modes of the down converted idler and signal photon, respectively. To detect the photons in the path Z basis (Logical base), we used the measurement system sketched in Figure 5.2.1 b). The output 4CF of the source is connected to a DM, coupling each core to a SMF. To detect photons propagating over the SMFs a home-made coincidence count system is used, which works as follows: a free-running trigger single

photon detector (Idquantique ID220) is connected to one of the SMFs, let's say the fiber 0 (associated to core 0) as shown in Figure 5.2.1 b), using a standard beam splitter (SMF-BS). When it registers a photon, a sync electrical pulse is sent to the four externally gated detectors (Idquantique ID210) for coincidence detections. These detectors are connected to the SMFs using optical delay lines such that coincidence counts can be registered using the sync signal. The ID210 detectors were configured with 25% detection efficiency, and 5 ns gate width, while the ID220 detector was configured with 15% detection efficiency and $5\mu s$ of dead time. To observe all of the sixteen possible coincidence events C_{jk}, the IDD220 was connected through a SMF-BS to each of the four SMFs, and counts of the form C_{j0}, C_{j1}, C_{j2}, C_{j3} were recorded for all values of j with an integration time of 5 s. For measurements in bases complementary to the Z basis, we first connected the output 4CF of the source to a 4CF-BS, as shown in Figure 5.2.1 c). The MCF output of the 4CF-BS was then routed through a DM and each core coupled again to the SMFs. The coincidence detection scheme was the same as in Figure 5.2.1 b). Including the relative phases corresponding to propagation in each core, the 4CF-BS allows us to measure in superposition bases of the form

$$\begin{aligned}
|0\rangle_D &= \frac{1}{2}\left(e^{i\phi_0}|0\rangle + e^{i\phi_1}|1\rangle + e^{i\phi_2}|2\rangle + e^{i\phi_3}|3\rangle\right) \\
|1\rangle_D &= \frac{1}{2}\left(e^{i\phi_0}|0\rangle + e^{i\phi_1}|1\rangle - e^{i\phi_2}|2\rangle - e^{i\phi_3}|3\rangle\right) \\
|2\rangle_D &= \frac{1}{2}\left(e^{i\phi_0}|0\rangle - e^{i\phi_1}|1\rangle + e^{i\phi_2}|2\rangle - e^{i\phi_3}|3\rangle\right) \\
|3\rangle_D &= \frac{1}{2}\left(e^{i\phi_0}|0\rangle - e^{i\phi_1}|1\rangle - e^{i\phi_2}|2\rangle + e^{i\phi_3}|3\rangle\right)
\end{aligned} \tag{5.3}$$

where $|j\rangle_D$ refers to the state at detector D_j after the 4CF-BS, and ϕ_j are the relative phases acquired over core j. One can switch between four mutually unbiased bases X_j, by choosing different values of the phases ϕ_j. In summary Table 5.2.1 are the specific phase for complementary. Beside, the X_j bases are mutually unbiased to the Z basis and also to each other.

Phase\ Base	X_0	X_1	X_2	X_3
ϕ_0	0	0	0	0
ϕ_1	0	π	$\pi/2$	$\pi/2$
ϕ_2	0	$\pi/2$	π	$\pi/2$
ϕ_3	0	$\pi/2$	$\pi/2$	π

Table 5.1: Phases ϕ_j of complementary X_j bases defined to measure in scenario c) of the Figure (5.2.1).

5.2.2 Source Characterization

Going into the purely experimental, the first thing to characterize was the nonlinear crystal. A setup was implemented with single mode optical fibers , the laser at 773 nm and an

optical system composed of the L_1 and L_2. The image of SMF was replicated in the center of crystal and couple into a point-like detector, composed of another SMF for 1550 nm connected directly to an ID210 detector. We scanned the crystal along the (transverse) horizontal (x) and vertical (y) axis, recording the corresponding detector single counts. In Figure (5.2.2) shown the spatial distribution of SPDC photons with crystal scanned in the y-direction. Similar results were obtained for the x-direction. An area of width $\sim 380\mu m$ with considerable single counts was identified. The generation zone found was contrasted with the distance between the most distant cores (More details in appendix C.2), choosing the magnification factor 4.5 such that the image size of the 4CF at the PPLN crystal was $\sim 350\mu m$. In this way, the crystal generates photon pairs in the four different illuminated regions defined by the image of the 4CF.

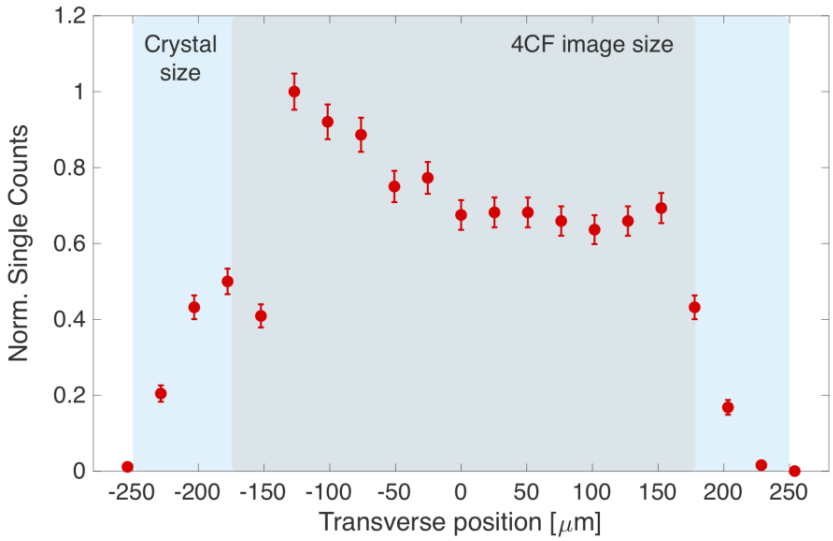

Figure 5.3: Normalized single-counts while scanning the vertical (y-axis) transverse direction of the PPLN crystal recorded by a point-like single-photon detector. The shaded regions correspond to the dimensions of the crystal and the image size of the 4CF.

The next parameter to characterize was the temperature for achieve the quasi-phase matching conditions, we tested that the optimal temperature was the same for each of the regions corresponding to the four cores. We adjusted the PPLN crystal temperature by placing it in an electronically-controlled oven. Figure (5.2.2) shows coincidence counts in each core, as a function of the temperature, recorded using the measurement scheme of (5.2.1 b). We observe that at 112^oC, a nearly optimized coincidence rate of SPDC in all cores was reached, in correspondence with the pump and down-converted photon wavelengths and the crystal poling period ($19.8\mu m$).
velengths and the crystal poling period (19.8 µm). Brightness of the source is an important characteristic, if entanglement is to be distributed over long-distances through

optical fibers. Our entanglement source operates with a pump laser power of $1mW$ per core. Taking this into account, plus the insertion losses of the optical devices and detector efficiencies ($\sim 4\%$ in coincidence) , the observed spectral brightness of the source was ~ 350000 photons pairs (s mW nm)$^{-1}$,which is comparable to optimized sources for polarization entangled photons [18]. Considering the typical loss in multi-core optical fibers of 0.4 dB per km for 1550 nm, it would be possible to distribute multi-dimensional entanglement over at least ~ 75 km of fiber. Thus, this source can be readily employed to investigate the propagation of spatial entanglement over long multi-core fibers, which has yet to be realized.

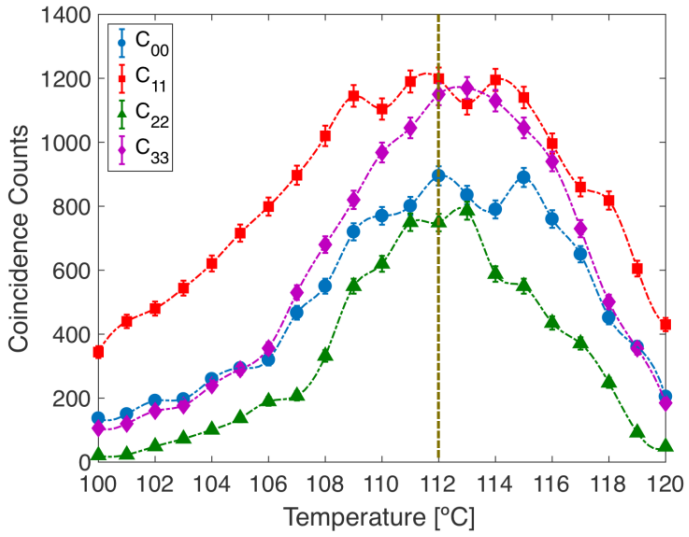

Figure 5.4: Coincidence rate in each core as a function of the crystal temperature. The optimal temperature to satisfy the phase-matching conditions for all cores is 112^oC.

Another remarkable feature of our source is the phase stability provided by coupling the pump and down converted light directly in and out of 4CFs, which are inherently robust against thermal fluctuations and mechanical stress since the cores lie within the same cladding [70, 43]. The relative phase between two different cores of a MCF can be at least two orders of magnitude more stable than two single-mode fibers over a 2km length [70]. When the X_j measurement bases are implemented, the last 4CF-BS combines together the incoming down converted photons, forming an interferometer that is sensitive to phase fluctuations. Thanks to the stability of the 4CF, without any fiber isolation system or active phase stabilization, we observe that phase oscillations typically occur with a period of several minutes. Figure 5.5 a) the coincident counts oscillator record and which are then used to 5.5 b) to get the absolute value of the frequency spectrum . The peaks of these distributions correspond to oscillations with period between 2 and 6.5 minutes. We can see in 5.5 b) that there are essentially no frequencies components above 0.008 Hz. Our goal here is to present the fundamental characteristics of the source but we note that, if necessary, one can employ the technique of reference [72] to phase-lock the source.

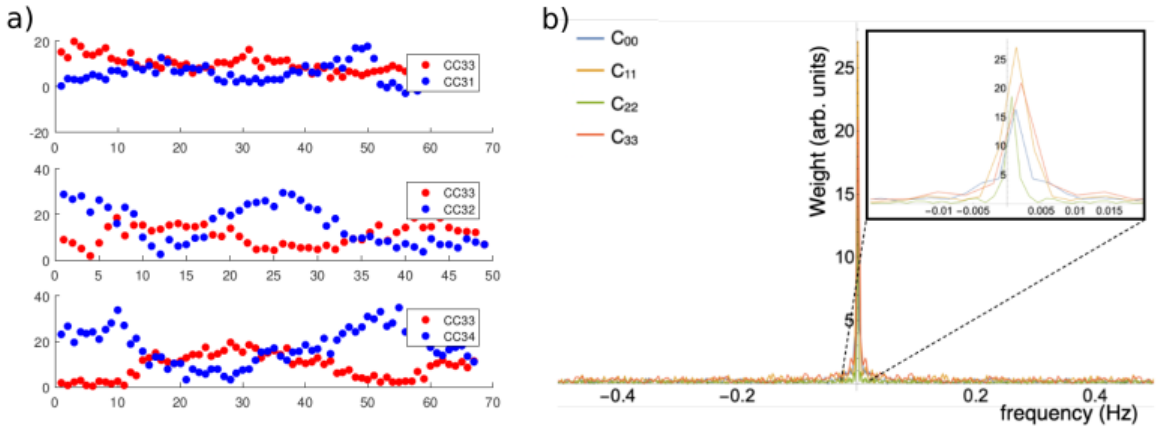

Figure 5.5: a) Example of coincidence counts oscillation of four of sixteen probabilities, with C_{33} as reference and recording C_{3i} $(i = 1, 2, 3)$ coincidence counts. b) Spectrum of frequency components of the coincidence counts between different detectors using detection system 5.2.1 c), taken at different times. Fluctuations due to phase changes occur on a time scale of several minutes.

5.2.3 Entanglement certification

We measured coincidence counts C_{jk} as was explained in section 5.2.1. Accidental coincidence counts a_{jk} arising from dark counts and ambient light were evaluated by recording the average count rate with a large relative electronic delay between detectors. The corrected coincidence counts, given by $C^c_{jk} = C_{jk} - a_{jk}$, were used to estimate the joint probability distributions: $P_{jk} = C^c_{jk} / \sum_{jk} C^c_{jk}$. Experimental error was calculated by assuming Poissonian count statistics and Gaussian error propagation. The recorded probability distributions while measuring both photons in the Z basis is shown in 5.6 a), with photons always found in the same core.
For measurements in the X_j bases, there are two photon coalescence effects on the 4CF-BS that impose a convenient symmetry to the coincidence counts. By considering the state of 5.2 and the measurements of equations 5.3, we see that the coincidence count probabilities at detectors $j, k (j, k = 0, 1, 2, 3)$ are given by

$$P^{the}_{jk} = \left| \frac{1}{8} \sum_{m=0}^{3} u_{mj} u_{mk} e^{i2\phi_m} \right|^2 \tag{5.4}$$

where the symbols u_{mj} and u_{mk} are the elements of the 5.1 matrix. In this case, when the relative phases are such that complete constructive/destructive interference occurs, only 4 of the 16 probabilities P_{mn} are non-zero. For example, when all of the phases are equal, the four probabilities $P_{00} = P_{11} = P_{22} = P_{33} = 1/4$. Since these four probabilities sum to one, all the rest are zero. This case corresponds to detection of both photons in the X_0 basis. For the phases corresponding to the X_1 basis, only probabilities $P_{01} = P_{10} = P_{23} = P_{31} = 1/4$ are non-zero. Likewise, for the X_2 basis we have $P_{02} = P_{20} = P_{13} = P_{31} = 1/4$ and all others equal to zero, while for X_3 we have $P_{03} = P_{30} = P_{12} = P_{21} = 1/4$ with the rest equal to zero. In this fashion, observing a maximum in one coincidence count group while

observing all of the others near zero allows us to identify the relative phase values.
The measurements in the X_i bases were identified using the coincidence count signatures described above, while applying a controlled bending to the 4CF fiber at the output of the source, causing mechanical stress that changes the relative phases between cores [85]. The joint probability distributions obtained from the four Xi measurements are shown in Figure 5.6 The similarity, C_B, of the recorded and theoretical probability distributions can be quantified using the Bhattacharyya coefficient [86]. In our case, it reaches $C_B = 0.91 \pm 0.02$, showing good agreement between theory and experiment.

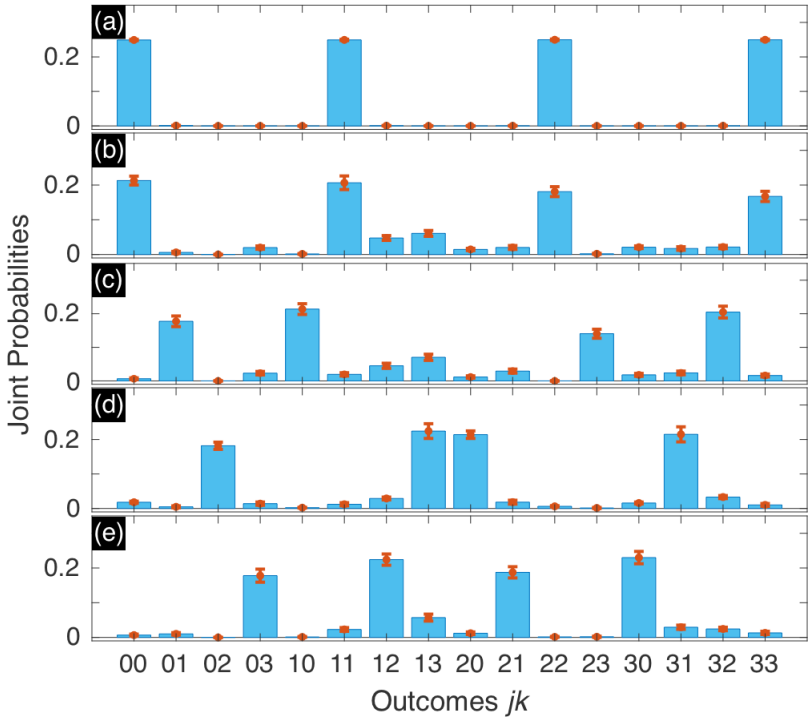

Figure 5.6: Joint probability distributions obtained while measuring both photons in the (a) Z basis, (b) X_0 basis, (c) X_1 basis, (d) X_2 basis, and (e) X_3 basis. Error bars are obtained considering Gaussian error propagation and Poissonian photo-count statistics.

1. *Fidelity*

To certify the multidimensional entanglement of the generated state ρ, we use its fidelity $F(\rho, |\Psi\rangle) = \langle\Psi|\rho|\Psi\rangle$ to the target state $|\Psi\rangle$ in equation 5.2. Is give by

$$F(\rho, |\Psi\rangle) = \sum_{j=0}^{3} \langle jj|\rho|jj\rangle + 2 \sum_{j=0,k=j+1}^{3} Re\left[\langle jj|\rho|kk\rangle\right] \tag{5.5}$$

where the first term is the measurement in $Z-$basis and is $P_{jj} = \langle jj|\rho|jj\rangle$. The second term is for coherence between state $|jj\rangle$ and $|kk\rangle$. These can be calculated by defining Pauli operators for the j, k subspace as [87, 88]: $\sigma_x^{(jk)} = |j\rangle\langle k| + |k\rangle\langle j|$, $\sigma_y^{(jk)} = i|j\rangle\langle k| - i|k\rangle\langle j|$. Then, $Re\left[\langle jj|\rho|kk\rangle\right] = \left(\langle\sigma_x^{(jk)} \otimes \sigma_x^{(jk)}\rangle - \langle\sigma_y^{(jk)} \otimes \sigma_y^{(jk)}\rangle\right)/4$. These expectation values can be evaluated directly from the X_i measurements, as we describe in detail in the Appendix D. Using the recorded data of the 5 mutually unbiased measurements, we obtain $F = 0.789 \pm 0.007$. Since any state with $F(\rho, |\Psi\rangle) > 3/4$ is incompatible with a Schmidt number ≤ 3 [87, 88], we can confirm the four-dimensional nature of the entanglement produced by the source.

1. *High-Dimensional Steering*

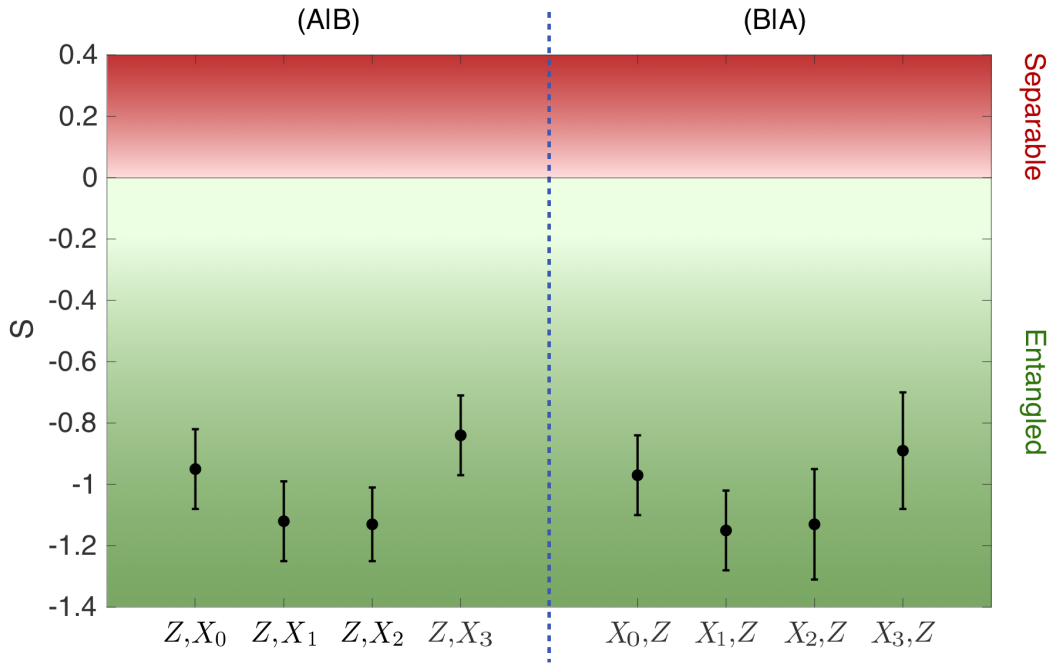

Figure 5.7: Experimental values for the EPR-steering criterion S for steering from A to B, denoted $(B|A)$ and from B to A, denoted $(A|B)$. When $S_{JK}^{(PQ)} < 0$ e can confirm that the state is entangled in the one-sided device independent scenario.

Another interesting approach to certify multi-level entanglement generation is the one based on quantum steering [89], which is a distinct correlation that lies between entanglement and Bell nonlocality, and has been related to one-sided device independent quantum cryptography [90], as well as one-sided device independent randomness generation [91, 92, 93, 19]. For two mutually unbiased bases corresponding to observables $\hat{P}$ and $\hat{Q}$, quantum steering can be identified using the entropic criterion [94]

$$S_{JK}^{(PQ)} = H(P_J|P_K) + H(Q_J|Q_K) - log_2(D) \geq 0 \tag{5.6}$$

where $J, K = A, B$ $(J \neq K)$ denote the subsystems. $H\left(P_J|Q_K\right)$ is the conditional Shannon entropy calculated over the joint probabilities associated to measurements in the P and Q bases on subsystems J and K, espectively. Steering can be an asymmetrical correlation, and violation of inequality (5.6) indicates steering from subsystem K to subsystem J when $S_{JK}^{(PQ)} < 0$, which also indicates that the two systems are entangled. Identifying $P = Z$ and $Q = X_j$, we applied these inequalities to our experimentally obtained probabilities of Figure (5.6). The conditional entropy was calculated using $H\left(P_J|Q_K\right) - H\left(Q_K\right)$, where $H\left(P_J|Q_K\right)$ is the joint Shannon entropy and $H\left(Q_K\right)$ is the marginal entropy corresponding to local measurement Q on part K. The results are shown in (5.7). We obtain negative values for all correlations tested, showing that the generated qudit state exhibits steering from A to B as well as from B to A. We obtained mean values $\overline{S}_{AB} = -1.01 \pm 0.06$ and $\overline{S}_{BA} = -1.04 \pm 0.08$. Identification of steering allows us to confirm that the generated state is entangled in a one-sided device independent scenario [53], meaning that full knowledge of the inner workings of one of the system's devices is not necessary. Moreover, the dimensionality of each subsystem can be observed through the Shannon entropies $H(P_J)$ and $H(Q_J)$ of the marginal distributions, which are all very close to the maximum value of $log_2 D = 2$ bits for D)4 dimensional subsystem, with mean value 1.99 ± 0.02 bits which is double the limit for $D = 2$ qubits systems.

Chapter 6

Conclusions

In this thesis it is present a new source of multidimensional photonic entanglement that is based on space-division multiplexing optical fibers, which makes it fully compatible with current and next generation telecommunications fiber networks. Furthermore, for our experiment used four multicore fibers, but this new design offers a scalability in numbers of cores. Given the geometry of the fibers and system optic with the crystal, we can reconnect other multicore and realignment an create other quantum state, this features provides a scenario of development, and widespread standards have yet to be established. In details, we prepare an entangled of two four-dimensional systems, encoded in the path degree of freedom of the down converted photons, and certify the multi-dimensional entanglement generation. Achieving the value of fidelity 0.789 ± 0.007, which make it incompatible with a Schmidt number ≤ 3 and with the probabilities having an average in Steering of $\overline{S}_{AB} = -1.01 \pm 0.06$ and $\overline{S}_{BA} = -1.04 \pm 0.08$ indicating entanglement in a one-sided device-independent scenario, checking the correlations of source.
The source presents several technical advantages, including high spectral brightness - comparable with modern polarization-entangled-qubit sources, and relatively long phase stability, thanks to the use of multi-core fibers. Consequently, our scheme has several potential applications. For instance, one can exploit the verified multi-dimensional steering for implementing one-side device independent quantum protocols such as quantum cryptography or quantum randomness generation [90, 91, 92, 93, 19]. The spectral brightness achieved of 350000 photon pairs generated $(s\ mW\ nm)^{-1}$, will allow for future investigations demonstrating the viability of long-distance distribution of multi-dimensional entanglement over multi-core fibers.
Finally, mention the actions or topics that cam be pointed with source. First, is implemented a system for control the phase and one option is realized in our laboratory [72]. Second, is take advantage of the source architecture to conduct research in quantum metrology exceed the standard quantum limit. In particular, the entangled state produced by our source is nearly optimal for multi-parameter phase estimation [96].

Appendix A

SPDC State

In the no linear material the electric polarization is given by

$$P_i(r,t) = \epsilon_0 \int_0^\infty dt' \chi_{ij}^{(1)}(t') E_j(r, t-t') + \int_0^\infty dt' \int_0^\infty dt'' \chi_{ijk}^{(2)}(t', t'') E_j(r, t-t') E_k(r, t-t''), \tag{A.1}$$

Where $E_j(r,t)$ are the components of the vector of the electric field. $\chi^{(1)}$ y $\chi^{(2)}$ are the electrical susceptibilities of the first and second order respectively. As the field strenght increases, the nonlinear terms increase in the equation (A.1). So, this analysis is focused until the second term.
We will start with Hamiltonian of the electromagnetic field in a dielectric medium of a volumen V.

$$\mathcal{H}(t) = \frac{1}{2} \int_V dr \left[D(r,t) \cdot E(r,t) + B(r,t) H(r,t) \right], \tag{A.2}$$

where **D** is the displacement vector, **B** is the induction magnetic and **H** is the magnetic field. Using the definition of $D(r,t) = \epsilon_0 E(r,t) + P(r,t)$ in the equation (A.2) we can rewrite of the following form

$$\mathcal{H}(t) = \mathcal{H}_0(t) + \mathcal{H}_I(t), \tag{A.3}$$

$\mathcal{H}_I$ is the no linear hamiltonian interaction, and the explicit formula is given by

$$\mathcal{H}_I(t) = \frac{1}{2} \int_V dr \int_0^\infty dt' \int_0^\infty dt'' \chi_{ijk}^{(2)}(t', t'') E_j(r, t-t') E_k(r, t-t''). \tag{A.4}$$

Now, we take the electric field and expand in functions of plane waves.

$$E(r,t) = E^+(r,t) + E^-(r,t), \tag{A.5}$$

with

$$E^+(r,t) = \frac{1}{\sqrt{\nu}} \sum_{k,\sigma} e_{k,\sigma} \varepsilon_{k,\sigma} \alpha_{k,\sigma} G(\omega) \cdot exp\left[i(k \cdot r - \omega t) \right], \tag{A.6}$$

where

$$\varepsilon_{k,\sigma} = \sqrt{\frac{\hbar\omega(k,\sigma)}{2\epsilon_0 n^2(k,\sigma)}}, \tag{A.7}$$

ϵ_0 is the permittivity in free space, $G(\omega)$ is the transfer function of the filters, ν is the quantization volume, k is the wave vector, $e_{k,\sigma}$ is the 2-dimensional of the polarization, ω is the frequency and $\alpha_{k,\sigma}$ is the mode amplitude. The usual method of quantization of electric field is chosen, where the amplitude mode $\alpha_{k,\sigma}$ is changed for $a_{k,\sigma}$, which is the annihilation operator. The, the electric field is

$$E^+(r,t) = \frac{1}{\sqrt{\nu}} \sum_{k,\sigma} \vec{e}_{k,\sigma}\varepsilon_{k,\sigma} a_{k,\sigma} G(\omega) \cdot exp\left[i(k \cdot r - \omega t)\right], \tag{A.8}$$

substituting (A.8) in (A.4)

$$\begin{aligned}\mathcal{H}_I(t) = \frac{1}{2\nu^{3/2}} \sum_{k_s,\sigma_s} \sum_{k_i,\sigma_i} \sum_{k_p,\sigma_p} g^*_{k_s,\sigma_s} g^*_{k_i,\sigma_i} g_{k_p,\sigma_p} a^\dagger_{k_s,\sigma_s} a^\dagger_{k_i,\sigma_i} a_{k_p,\sigma_p} exp\left[i(\omega_s + \omega_i - \omega_p)\right] \\ \times \chi_{ijk} (e_{k_s,\sigma_s})^*_i (e_{k_i,\sigma_i})^*_j (e_{k_p,\sigma_p})_k \int_\nu exp\left[-i(k_s + k_i - k_p) \cdot r\right] + H.C,\end{aligned} \tag{A.9}$$

where

$$g_{k_j,\sigma_j} = i\sqrt{\frac{\hbar\omega(k_j,\sigma_j)}{2\epsilon_0 n^2 \omega(k_j,\sigma_j)}} G\left[\omega(k_j,\sigma_j)\right], \tag{A.10}$$

H.C is the hermitian conjugate, $n\omega(k_j,\sigma_j)$ is the index of refraction of the crystal. In addition, terms that do not conserve energy are eliminated.

$$\chi_{ijk} \equiv \chi^{(2)}_{ijk}(\omega_p = \omega_s + \omega_i) + \chi^{(2)}_{ijk}(\omega_i = \omega_s + \omega_p) + \chi^{(2)}_{ijk}(\omega_s = \omega_p + \omega_i), \tag{A.11}$$

with

$$\chi^{(2)}_{ijk}(\omega = \omega' + \omega'') = \int_0^\infty dt' \int_0^\infty dt'' \chi_{ijk}(t', t'') exp\left[-(\omega' t' + \omega'' t'')\right], \tag{A.12}$$

we use the previous result of hamiltonian for calculate the state.

$$|\psi(t)\rangle = \hat{U}(t)|\Psi(0)\rangle, \tag{A.13}$$

$$\hat{U}(t) = exp\left(\frac{1}{i\hbar}\int_0^t dt' \hat{\mathcal{H}}(t')\right), \tag{A.14}$$

expanding the evolution operator in serie

$$\hat{U}(t) = 1 + exp\left(\frac{1}{i\hbar}\int_0^t dt' \hat{\mathcal{H}}(t')\right) + ..., \tag{A.15}$$

replacing (A.9) in the integral of the evolution operator, the integral is given by

$$\int_0^t dt' \hat{\mathcal{H}}(t') = \frac{1}{2\nu^{3/2}} \sum_{k_s,\sigma_s} \sum_{k_i,\sigma_i} \sum_{k_p,\sigma_p} g^*_{k_s,\sigma_s} g^*_{k_i,\sigma_i} g_{k_p,\sigma_p} a^\dagger_{k_s,\sigma_s} a^\dagger_{k_i,\sigma_i} a_{k_p,\sigma_p}$$
$$\times \chi_{ijk} exp\left[i(\omega_s + \omega_i - \omega_p)t/2\right] (e_{k_s,\sigma_s})^*_i (e_{k_i,\sigma_i})^*_j (e_{k_p,\sigma_p})_k$$
$$\times t \cdot sinc\left[(\omega_s + \omega_i - \omega_p)t/2\right] \int_V exp\left[(\omega_s + \omega_i - \omega_p) \cdot r\right] dr + H.C., \tag{A.16}$$

integrating in r

$$\int_0^t dt' \hat{\mathcal{H}}(t') = \frac{Vt}{2\nu^{3/2}} \sum_{k_s,\sigma_s} \sum_{k_i,\sigma_i} \sum_{k_p,\sigma_p} g^*_{k_s,\sigma_s} g^*_{k_i,\sigma_i} g_{k_p,\sigma_p} a^\dagger_{k_s,\sigma_s} a^\dagger_{k_i,\sigma_i} a_{k_p,\sigma_p}$$
$$\times \chi_{ijk} (e_{k_s,\sigma_s})^*_i (e_{k_i,\sigma_i})^*_j (e_{k_p,\sigma_p})_k \cdot sinc\left[(\omega_s + \omega_i - \omega_p)t/2\right]$$
$$\times exp\left[i(\omega_s + \omega_i - \omega_p)t/2\right] \prod_m sinc\left[(k_s + k_i - k_p)_m l_m/2\right]$$
$$\times exp\left[-i(k_s + k_i - k_p)_z l_z/2\right] + H.C., \tag{A.17}$$

where $V = l_x \times l_y \times l_z$ and l_m is the dimension of the no lineal medium in the direction m $(m = x, y, z)$. Reemplacing (A.17) in (A.13) and considering the initial state as the vacuum state.

$$|\psi(t)\rangle = |vac\rangle + \frac{Vt}{2i\hbar\nu^{3/2}} \sum_{k_s,\sigma_s} \sum_{k_i,\sigma_i} \sum_{k_p,\sigma_p} g^*_{k_s,\sigma_s} g^*_{k_i,\sigma_i} g_{k_p,\sigma_p} \upsilon_p(k_p,\sigma_p) \chi_{ijk}$$
$$\times (e_{k_s,\sigma_s})^*_i (e_{k_i,\sigma_i})^*_j (e_{k_p,\sigma_p})_k \cdot sinc\left[(\omega_s + \omega_i - \omega_p)t/2\right]$$
$$\times exp\left[(\omega_s + \omega_i - \omega_p)t/2\right] \prod_m sinc\left[(k_s + k_i - k_p)_m l_m/2\right]$$
$$\times exp\left[-i(k_s + k_i - k_p)_z l_z/2\right] |k_s,\sigma_s\rangle |k_i,\sigma_i\rangle, \tag{A.18}$$

where $|k_s,\sigma_s\rangle |k_s,\sigma_s\rangle$ are the Fock states in the modes k_j and σ_j, $\upsilon(k_p,\sigma_p)$ is the classic amplitude corresponding to the component (k_p,σ_p) of pump. Beside, to reach the final state we should consider some approximations.

- The interaction time is long enough, so that the $sinc(\omega_s + \omega_i = \omega_p)$ is significant only when $\omega_s + \omega_i = \omega_p$.
- The dispersion of the center frequency is very small and this is justified by the frecuency filters.
- The pump travel for the $Z - axis$ and the crystal is long enough on the x and y axes for contain all cross section .

- The pump just contains extraordinary polarization.

With these considerations we can write the final state for the no linear process SPDC.

$$|\Psi\rangle = \sum_{\sigma_s,\sigma_i} \int d\omega_s \int d\omega_i \int dq_s \int dq_i \Phi_{\sigma_s,\sigma_i}(q_s, q_i, \omega_s, \omega_i)|q_s, \omega_s, \omega_s\rangle|q_i, \omega_i, \omega_i\rangle, \tag{A.19}$$

the amplitude Φ is reduced to

$$\Phi \approx C_{\sigma_s\sigma_i} G_s(\omega_s) G_i(\omega_i) \nu(q_s + q_i, \omega_s + \omega_i) sinc\left[(K_{sz} + K_{iz} - K_p z)L/2\right], \tag{A.20}$$

where $C_{\sigma_s\sigma_i}$is the coupling constant, which depends of the nonlinear susceptibility. $G_s(\omega_s)$ y $G_i(\omega_i)$ are the functions defined for the interference filters used in front of detectors.

Appendix B

SDM devices characterization

In this appendix we will deepen the characterization of beam splitter multicore and show de split ratios. In the tables that will be shown below you will see the powers used and the percentages obtained for each combination that can be done with with a four paths Beam splitter multicore.
The measurements were made at four BS-MCF with a continuous laser of 775nm and the challenge is find the best beam splitter because the fibers that was build the beam splitter are for 1550nm.

B.1 Experimental setup

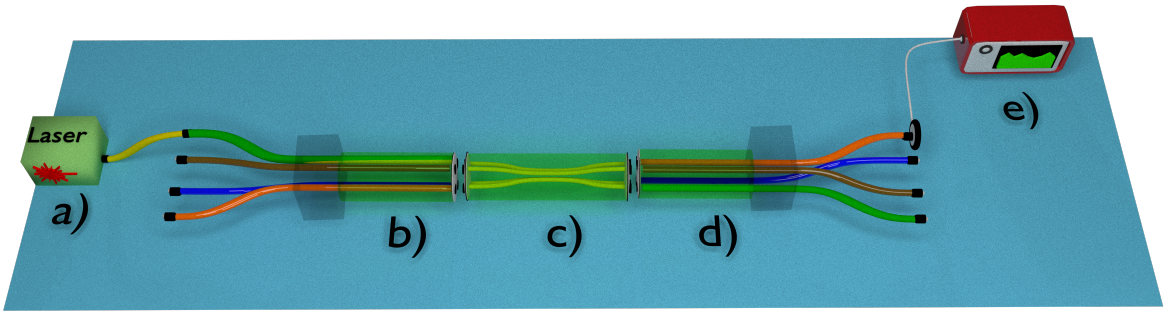

Figure B.1: Experimental setup of characterization of beam splitter multicore. a) Continuous laser of 775nm. b) Input demultiplexer where each color represent one core of multicore fibre. c) Beam splitter multicore of four cores. d) Output multiplexer. e) Power meter. Source: Made by author.

Experimental setup consist in five parts (See details in Figure B.1) and start with a continuous laser tunable Lion *TEC500* at 773nm, this laser is connected to the input

demultiplexer, this is how we access a particular core. After, demux is connected to the BS-MCF and this is connected to the output demultiplexer. Finally, the system is measured by the power meter.
The technical characteristics of the multicore fibres is a diamond shaped with four core of $8\mu m$ of diameter, $50\mu m$ of distance between the closest neighbors and $70.7\mu m$ for the farthest. Furthermore, each color of fibres in demultiplexer represent each core, this adds ease to illuminate each core.

B.2 Demultiplexer characterization

Prior to measuring the complete system, the first step was measure the split ratio of the demultiplexer (Built to $1550nm$) with continuous laser $773nm$. Specifically, each single core fiber was connected to the laser, and together with that, the power meter was connected to input demultiplexer from the multicore side. The following table show the transmission results for each core for demultiplexer letter a), this percent is analogous for output demultiplexer.

Core	Power input $[mW]$	Power output $[mW]$	Transmission (%)
1	17.3	14.36	86
2	17.5	14.63	84
3	17.5	14.52	83
4	17.45	15.95	91

Table B.1: Characterization of the 1550 nm demultiplexer with continuous laser to $773nm$.

B.3 Beam splitters multicore characterization

The procedure to measure the BS-MCFs was make all combinations possible between input demultiplexar and output demultiplexer. We generate sixteen split ratios for each beam splitter and the best result we tried it in opposite direction.
The split ratio formula consider each power core and sum of all of them.

$$Sr_m = \frac{C_m}{C_1 + C_2 + C_3 + C_4} \times 100 = \frac{C_m}{\sum_{i=1}^{4} C_i} \times 100 \tag{B.1}$$

where C_m is the specific core, and split ratio show in table and $m = 1, 2, 3, 4$ for our case. Below are the summary tables obtained from the measurement process. The BS-MCF are labeled as $BS - MCF - i$, with $i = 1, 2, 3, 4$.

In summary, from the tables shown it was possible to choose the best A and its path that has the best split ratios of each core. The beam splitter number four was one the best numbers and we prove in the opposite directions and after connect to experimental setup.

BS-MCF-1					
Input core	Power input [mW]	Power output [mW]		Power total [mW]	Split ratio (%)
		C_1	1.96		29.56
C_1	31	C_2	1.47	6.63	22.17
		C_3	1.76		26.55
		C_4	1.44		21.72
		C_1	2.65		32.00
C_2	31	C_2	2.23	8.28	26.93
		C_3	2		24.15
		C_4	1.4		16.91
		C_1	1.62		21.37
C_3	30.9	C_2	2.41	7.58	31.79
		C_3	1.72		22.69
		C_4	1.83		24.14
		C_1	2.29		24.76
C_4	31.3	C_2	2.89	9.25	31.24
		C_3	1.83		19.78
		C_4	2.24		24.22
BS-MCF-2					
Input core	Power input [mW]	Power output [mW]		Power total [mW]	Split ratio (%)
		C_1	0.75		24.12
C_1	31	C_2	0.61	3.11	19.61
		C_3	0.75		24.12
		C_4	1		32.15
		C_1	1.4		29.47
C_2	31.1	C_2	1.66	4.75	34.95
		C_3	0.7		14.74
		C_4	0.99		20.84
		C_1	2.51		20.57
C_3	31.3	C_2	2.57	12.2	21.07
		C_3	3.72		30.49
		C_4	3.4		27.87
		C_1	3.43		32.45
C_4	31.2	C_2	2.96	10.57	28.00
		C_3	2		18.92
		C_4	2.18		20.62

Table B.2: Summary table of experimental result for BS-MCF-1 and BS-MCF-2

BS-MCF-3					
Input core	Power input [mW]	Power output [mW]		Power total [mW]	Split ratio (%)
		C_1	1.53		20.08
C_1	31	C_2	2.26	7.62	29.66
		C_3	1.52		19.95
		C_4	2.31		30.31
		C_1	1.59		19.85
C_2	31.1	C_2	2.49	8.01	31.09
		C_3	1.62		20.22
		C_4	2.31		28.84
		C_1	2.7		23.79
C_3	31	C_2	2.71	11.35	23.88
		C_3	3.2		28.19
		C_4	2.74		24.14
		C_1	4.75		31.13
C_4	31.4	C_2	3.66	15.26	23.98
		C_3	3.6		23.59
		C_4	3.25		21.30
BS-MCF-4					
Input core	Power input [mW]	Power output [mW]		Power total [mW]	Split ratio (%)
		C_1	0.64		14.61
C_1	30.7	C_2	1.17	4.38	26.71
		C_3	1.17		26.71
		C_4	1.4		31.96
		C_1	2.11		22.00
C_2	30.6	C_2	3.2	9.59	33.37
		C_3	1.98		20.65
		C_4	2.3		23.98
		C_1	2.6		22.75
C_3	30.7	C_2	2.64	11.43	23.10
		C_3	3.39		29.66
		C_4	2.8		24.50
		C_1	4.9		33.02
C_4	30.8	C_2	3.58	14.84	24.12
		C_3	3.45		23.25
		C_4	2.91		19.61

Table B.3: Summary table of experimental result for BS-MCF-3 and BS-MCF-4

BS-MCF-4 inverted					
Input core	Power input [mW]	Power output [mW]		Power total [mW]	Split ratio (%)
		C_1	0.5		9.38
C_1	30.9	C_2	1.7	5.33	31.89
		C_3	1.31		24.58
		C_4	1.82		34.15
		C_1	1.42		17.86
C_2	30.3	C_2	3	7.95	37.74
		C_3	1.43		17.99
		C_4	2.1		26.42
		C_1	2		22.47
C_3	31.1	C_2	2.1	8.9	23.60
		C_3	2.7		30.34
		C_4	2.1		23.60
		C_1	2		25.22
C_4	30.8	C_2	2.42	7.93	30.52
		C_3	1.51		19.04
		C_4	2		25.22

Table B.4: Summary table of experimental result for BS-MCF-4 inverted

Appendix C

Programming scripts

Sometimes, in optic systems it is necessary quantify parameters like magnifications or distances, to be compared with theoretical results, so below is how part of the image post-processing was done. Here, are the scripts used for measure the size of Gaussian shape generated for single mode fibers or distant between of two (or more) pixels, that is euclidean distance. All codes were written in open source code Python.

C.1 Gaussian fit to pump from the camera image

First, is to save the image created by the optical system. The camera used was DCC1645C-HQ from Thorlabs.

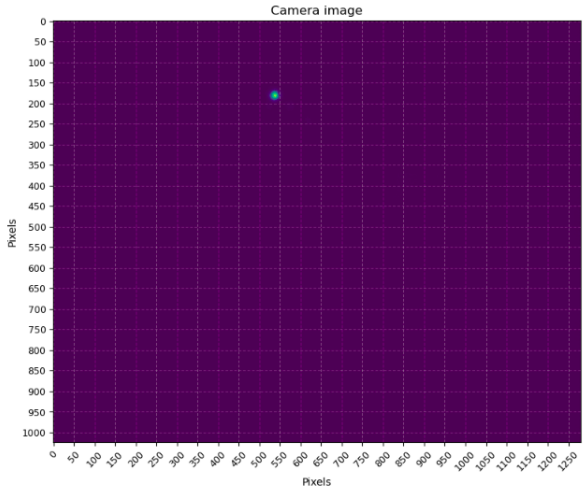

Figure C.1: Image of Gaussian beam of single mode fiber. Source: Made by author.

The next step is that find the pixel with maximum brihtness and in function this define

cross profiles of x axis and y axis respectively. The bound of image can be defined by the user.

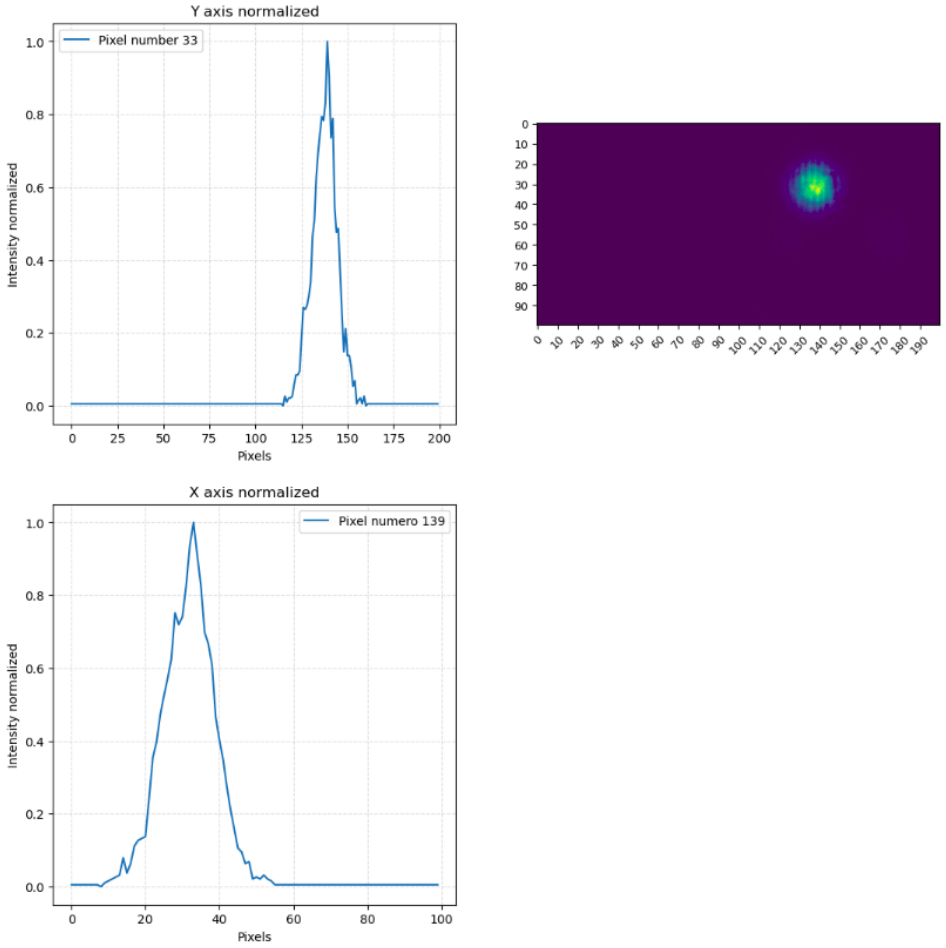

Figure C.2: Cross section of both axis of Gaussian beam. The color range was normalized. Source: Made by author.

Finally, based on data, perform the fit of a Gaussian function (equation C.1). Furthermore, is calculated the mode field diameter (MFD)[1] and the parameter r^2 in both axis

$$f(x, a, b, c, d) = exp\left(\frac{-2(x-b)^2}{c^2}\right) + d, \tag{C.1}$$

where a is a peak of profile, b where is centered, c is bandwidth, d is the displacement of the origin in y axis and x is fit range. This scripts work with seed values, so the parameter

[1]In single mode fiber, the shape of beam is maintains and is near to Gaussian shape. The mode field diameter describe the width of this intensity profile. Then, the intensity in profile decrease in e^2 respect to the peak, is the MFD.

a, b, c d must be write and scripts find the optimal values for the fit. The final result of fit in Figure C.3. Furthermore, the script calculate the r^2 from *Sklearn* package, that for this example was 0.9903 for x axis and 0.9848 for y axis, showing the good implementation of the fit.

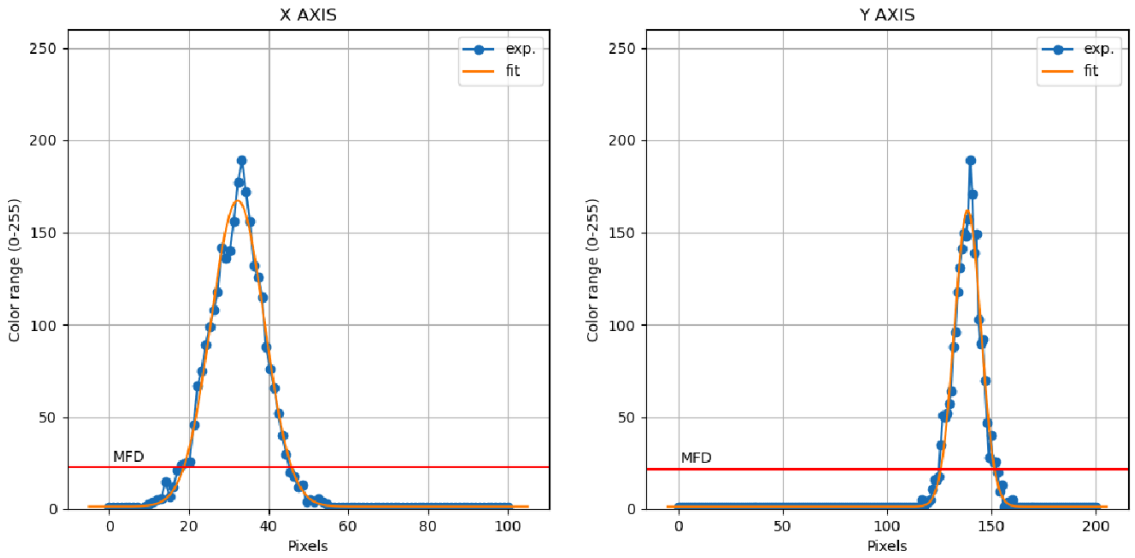

Figure C.3: Experimental data an Gaussian fit to image. The blue points is experimental data, the solid orange line is Gaussian fit and the red line marks the MFD, i.e the decrease of the peak by a factor of e^{-2}. Source: Made by author.

```
from scipy import ndimage
import imageio
import numpy as np
from matplotlib.pyplot import*
from scipy.optimize import leastsq
from scipy.optimize import curve_fit
from sklearn.metrics import r2_score
import statistics

image =imageio.imread('Testimage.tif')
Sizeplot=20
im0=image[:,:,1]
fig =figure(figsize=(Sizeplot,Sizeplot))
subplot(221)
imshow(im0)
xlabel('Pixels')
ylabel('Pixels')
yticks(np.arange(0, im0.shape[0], 50),size=9)
xticks(np.arange(0, im0.shape[1], 50), rotation=45,size=9)
title('Camera image')
grid(linestyle='--',alpha=0.5)
show()
x1 = int(input("Upper limit in Y axis (Pixel): "))          #Upper limit
x2 = int(input("Lower limit in Y axis (Pixel): "))          #Lower limit
```

```
y1 = int(input("Upper limit in X axis (Pixel): "))          #Left limit
y2 = int(input("Upper limit in X axis (Pixel): "))          #Right limit
zoom = im0[x1:x2,y1:y2]
imshow(zoom)
yticks(np.arange(0, zoom.shape[0], 10),size=9)
xticks(np.arange(0, zoom.shape[1], 10), rotation=45,size=9)
show()
a=np.where(zoom == zoom.max())
option=2
if option==1:
    X=zoom[:,a[1][1]]        # Array that contains a maximum
    Perfilnormx=X/max(X)     # Cross-section but is normalized
    pixelesx=range(len(X))
    Y= zoom[a[0][1],:]
    Perfilnormy=Y/max(Y)
    pixelesy=range(len(Y))
    fig =figure(1,figsize=(13,13))
############CROSS SECTION IN X
    subplot(221)
    plot(pixelesy,Perfilnormy,label='Pixel number '+str(a[0][1]))
    legend(loc=0)
    xlabel('Intensity normalized')
    ylabel('Color range')
    title('X axis normalized')
    grid(linestyle='--',alpha=0.4)
############
    subplot(222)
    imshow(zoom)
    yticks(np.arange(0, zoom.shape[0], 10),size=9)
    xticks(np.arange(0, zoom.shape[1], 10), rotation=45,size=9)
############CROSS SECTION IN Y
    subplot(223)
    plot(pixelesx,Perfilnormx,label='Pixel number '+str(a[1][1]))
    legend(loc=0)
    xlabel('Pixels')
    ylabel('Intensity normalized')
    title('Y axis normalized')
    grid(linestyle='--',alpha=0.4)
    show()
elif option==2:
    X=zoom[:,a[1][0]]        # Array that contains a maximum
    Perfilnormx=X/max(X)     # Cross-section, but is normalized
    pixelesx=range(len(X))
    Y= zoom[a[0][0],:]       # Array that contains a maximum
    Perfilnormy=Y/max(Y)     # Cross-section but is normalized
    pixelesy=range(len(Y))
    fig =figure(1,figsize=(13,13))
############CROSS SECTION IN X
    subplot(221)
    plot(pixelesy,Perfilnormy,label='Pixel number '+str(a[0][0]))
    legend(loc=0)
    xlabel('Pixels')
    ylabel('Intensity normalized')
    title('Y axis normalized')
```

```
    grid(linestyle='--',alpha=0.4)
#############
    subplot(222)
    imshow(zoom)
    yticks(np.arange(0, zoom.shape[0], 10),size=9)
    xticks(np.arange(0, zoom.shape[1], 10), rotation=45,size=9)
#############CROSS SECTION IN Y
    subplot(223)
    plot(pixelesx,Perfilnormx,label='Pixel number '+str(a[1][0]))
    legend(loc=0)
    xlabel('Pixels')
    ylabel('Intensity normalized')
    title('X axis normalized')
    grid(linestyle='--',alpha=0.4)
    show()
#############FIT X AXIS
bandx= 7#std(X,ddof=1)
x= np.linspace(0,len(X),len(X))
def eps1(p,x):
    return func1(x,p[0],p[1],p[2],p[3])-X
parametros1=[max(X),int(np.mean(a[0])),bandx,min(X)]
(anchox,bx,cx,dx),_=leastsq(eps1,parametros1,args=(x))
print('ax opt.= '+str(round(anchox,2))+'| ax input:'+str(max(X))        )
print('bx opt.= '+str(round(bx,2))+'| bx input:'+str(int(np.mean(a[1]))))
print('cx opt.= '+str(round(cx,2))+'| cx input:'+str(round(bandx))      )
print('dx opt.= '+str(round(dx,2))+'| dx input:'+str(min(Y))            )
#############FIT Y AXIS
bandy= 7
y= np.linspace(0,len(Y),len(Y))
def eps0(p,x):
    return func1(x,p[0],p[1],p[2],p[3])-Y
parametros0=[max(Y),int(np.mean(a[1])),bandy,min(Y)]
(anchoy,by,cy,dy),_=leastsq(eps0,parametros0,args=(y))
print('ay opt.= '+str(round(anchoy,2))+'| ay input:'+str(max(Y))      )
print('by opt.= '+str(round(by,2))+'| by input:'+str(int(np.mean(a[0]))))
print('cy opt.= '+str(round(cy,2))+'| cy input:'+str(round(bandy))    )
print('dy opt.= '+str(round(dy,2))+'| dy input:'+str(min(Y))          )
##############Functions
extension=5
xx1=np.linspace(0-extension,len(X)+extension,2000)
xx2=np.linspace(0-extension,len(Y)+extension,2000)
Gaussx=func1(xx1,anchox,bx,cx,dx)
Gaussy= func1(xx2,anchoy,by,cy,dy)
MFDx=round(max(Gaussx*(1/np.e**2)),2)
MFDy=round(max(Gaussy*(1/np.e**2)),2)
#############PLOTFITS
fig =figure(1,figsize=(13,13))
subplot(221)
plot(x,X,'o-',label='Exp.')
plot(xx1,Gaussx,label='Fit')
grid()
xlabel('Pixels')
ylabel('Color range (0-255)')
title('X AXIS')
```

```
text(1, MFDx+3, 'MFD', fontdict=None)
axhline(y = MFDx, color = 'r', linestyle = '-')
ylim(0,260)
legend(loc=0)

subplot(222)
plot(y,Y,'o-',label='Exp.')
plot(xx2,Gaussy,label='Fit')
grid()
xlabel('Pixels')
ylabel('Color range (0-255)')
text(1, MFDy+3, 'MFD', fontdict=None)
axhline(y = MFDy, color = 'r', linestyle = '-')
title('Y AXIS')
legend(loc=0)
ylim(0,260)
nameimg=input('Write the name of image: ')
savefig('Image/'+str(nameimg)+'.png')
show()
#############R-SQUARE X AXIS
xx= np.linspace(0,len(X),len(X))
rsquarex = r2_score(X,func1(xx,anchox,bx,cx,dx))
print('R-square in X axis is: '+str(round(rsquarex,4)))
#############R-SQUARE Y AXIS
yy= np.linspace(0,len(Y),len(Y))
rsquarey =r2_score(Y, func1(yy,anchoy,by,cy,dy))
print('R-square in Y axis: '+str(round(rsquarey,4)))
print("The MFD of x-axis is in y="+ str(MFDx))
print("The MFD of y-axis is in y="+ str(MFDy))
```

Listing C.1: Script for analyze the image and create a fit on experimental data.

C.2 Euclidean distance between two pixels

An 1 : 1 optical system was set up and we illuminated the four core with demultiplexer and MCF-BS for create the image. Furthermore, we used a DCC1645C-HQ camera for capture the core image. 4-core image in C.4.

The Euclidean formula $D = \sqrt{(P_{x_2} - P_{x_1})^2 + (P_{y_2} - P_{y_1})^2}$ we used for calculate the distance between cores, where P_{x_i} and P_{y_i} $(i = 1, 2)$ are the coordinates of the saved pixels. The distance results is in pixels numbers, so we must multiply it by $3.6\mu m$, that is pixel size for this camera model.

Figure C.4: 4-Core image camera. Optical image of multicore fiber and used for analysis. Source: Made by author.

```
1
2  from scipy import ndimage, misc
3  from numpy import*
4  from matplotlib.pyplot import*
5
6  import imageio
7  image = imageio.imread('Testimage.tif')
8  im0=image[:,:,0]
9  fig =figure(figsize=(12,12))
10 subplot(222)
11 imshow(im0)
12 xlabel('Pixeles')
13 ylabel('Pixeles')
14 yticks(arange(0, im0.shape[0], 50),size=9)
15 xticks(arange(0, im0.shape[1], 50), rotation=45,size=9)
16 title('Camera plane')
17 grid(linestyle='--',alpha=0.4)
18
19 subplot(221)
20 imshow(image)
21 title('Original image')
```

```
xlabel('Pixeles')
ylabel('Pixeles')
show()
savefig('Safeimage.png')

x1 = int(input("Upper limit in y-axis (in pixels): "))
x2 = int(input("Low limit in y-axis (in pixels): "))
y1 = int(input("Left limit in x-axis (in pixels): "))
y2 = int(input("Right limit in x-axis (in pixels):"))
zoom = im0[x1:x2,y1:y2]
imshow(zoom)
""" Numbers of cliks """
def onclick(event):
    global ix, iy
    ix, iy = event.xdata, event.ydata
    # assign global variable to access outside of function
    global coords
    coords.append((ix, iy))

    # Disconnect after 2 clicks
    if len(coords) == 2: #number of click
        fig.canvas.mpl_disconnect(cid)
        close(10)
    return
coords = []

fig =figure(10)
cid = fig.canvas.mpl_connect('button_press_event', onclick)
imshow(zoom)
show()
f = array(coords , dtype = float64)
print(f)
distp = sqrt((f[1][0]-f[0][0])**2 + (f[1][1]-f[0][1])**2)
distm=distp*3.6
print('Distance between pixels (micrometers):'+ str(distm))
input("Press Enter to continue")
```

Listing C.2: Script for distance of two pixels. The number of clicks (2) and size of pixel camera ($3.6\mu m$) is tunable.

Appendix D

Fidelity calculation from probability distributions

The fidelity was calculated from the experimental data by defining the Pauli operators for the j, k subspace as [87, 88]: $\sigma_x^{(jk)} = |j\rangle\langle k| + |k\rangle\langle j|$, $\sigma_y^{(jk)} = i|j\rangle\langle k| - i|k\rangle\langle j|$. Then, $Re\left[\langle jj|\,\rho\,|kk\rangle\right] = \left(\langle\sigma_x^{(jk)} \otimes \sigma_x^{(jk)}\rangle - \langle\sigma_y^{(jk)} \otimes \sigma_y^{(jk)}\rangle\right)/4$. Let us denote the probabilities from the X_j measurements as $P^{(j)} = \{P_{xy}^{(j)}\}$, with x, $y = 0, ..., 3$. We also define the correlation functions

$$\begin{aligned} C_j(\alpha,\beta,\gamma,\delta) &= P_{\alpha\alpha}^{(j)} + P_{\alpha\beta}^{(j)} + P_{\beta\alpha}^{(j)} + P_{\beta\beta}^{(j)} + P_{\gamma\gamma}^{(j)} + P_{\gamma\delta}^{(j)} + P_{\delta\gamma}^{(j)} + P_{\delta\delta}^{(j)} \\ &- P_{\alpha\gamma}^{(j)} - P_{\alpha\delta}^{(j)} - P_{\alpha\gamma}^{(j)} - P_{\alpha\delta}^{(j)} - P_{\gamma\beta}^{(j)} - P_{\gamma\beta}^{(j)} - P_{\delta\beta}^{(j)} - P_{\delta\beta}^{(j)} \end{aligned} \tag{D.1}$$

for α, β, γ, $\delta = 0, 1, 2, 3$. Then, it is a straightforward but lengthy calculation to show that we can use the X_j measurement probability distributions in the above correlation function to determine the terms in the Fidelity. Explicitly, we have

$$\begin{aligned} 2Re\left[\langle 00|\,\rho\,|11\rangle\right] + 2Re\left[\langle 22|\,\rho\,|33\rangle\right] &= \frac{1}{4}[C_0(0,1,2,3) + C_1(0,1,2,3) \\ &- C_2(0,1,2,3) - C_3(0,1,2,3)] \end{aligned} \tag{D.2}$$

$$\begin{aligned} 2Re\left[\langle 00|\,\rho\,|22\rangle\right] + 2Re\left[\langle 11|\,\rho\,|33\rangle\right] &= \frac{1}{4}[C_0(0,2,1,3) + C_1(0,2,1,3) \\ &- C_2(0,2,1,3) - C_3(0,2,1,3)] \end{aligned} \tag{D.3}$$

$$\begin{aligned} 2Re\left[\langle 00|\,\rho\,|33\rangle\right] + 2Re\left[\langle 11|\,\rho\,|22\rangle\right] &= \frac{1}{4}[C_0(0,3,1,2) + C_3(0,3,1,2) \\ &- C_1(0,3,1,2) - C_2(0,3,1,2)] \end{aligned} \tag{D.4}$$

These expressions can be used directly in equation (5.5) to calculate the fidelity.

References

[1] Ehrenfest P., Welche Züge der Lichtquantenhypothese spielen in der Theorie der Wärmestrahlung eine wesentliche Rolle?, *Annalen der Physik.*, 341, 11, 1911.

[2] Einstein, A., B. Podolsky, and N. Rosen, Can Quantum-Mechanical Description of Physical Reality Be Considered Complete?, *Phys. Rev.*, 47, 777, 1935.

[3] Bell, J. S., On the Einstein Podolsky Rosen paradox, *Physics (Long Island City, N.Y.)*, 1, 195, 1964.

[4] Shor, P. W., Polynomial-time algorithms for prime factorization and discrete logarithms on a quantum computer, *SIAM J. Sci. Stat. Comput.*, 26, 1484, 1997.

[5] Alain Aspect, Philippe Grangier, and Gérard Roger, Experimental Tests of Realistic Local Theories via Bell's Theorem, *Phys. Rev. Lett.*, 47, 460, 1981.

[6] Alain Aspect, Jean Dalibard, and Gérard Roger, Experimental Test of Bell's Inequalities Using Time-Varying Analyzers, *Phys. Rev. Lett.*, 49, 1804, 1982.

[7] L. K. Grover, A fast quantum mechanical algorithm for database search, *Proceedings of the 28th Annual ACM Symposium on the Theory of Computing*, 1996.

[8] Feynman, R., Simulating physics with computers, *Int. J. Theor. Phys.*, 21, 467, 1982.

[9] Wootters, W. K. and Zurek, W. H, A single quantum cannot be cloned, *Nature*, 299, 802-803, 1982.

[10] Stephen M. Barnett and Sarah Croke. Quantum state discrimination. *Adv. Opt. Photon.*, 1(2):238–278, Apr 2009.

[11] C. H. Bennett and G. Brassard. Quantum cryptography: Public key distribution and coin tossing. *In Proceedings of IEEE International Conference on Computers, Systems and Signal Processing*, 175:010402, Dec 1984.

[12] Dik Bouwmeester, Jian-Wei Pan, Klaus Mattle, Manfred Eibl, Harald Weinfurter, and Anton Zeilinger. Experimental quantum teleportation. *Nature*, 390(6660):575–579, Dec 1997.

[13] Louis Broglie. *Recherches sur la théorie des Quanta*. PhD thesis, Université encours d'affectation, 1924.

[14] Artur K. Ekert. Quantum cryptography based on bell's theorem. *Phys. Rev. Lett.*, 67:661–663, Aug 1991.

[15] S. Friberg, C. K. Hong, and L. Mandel. Measurement of Time Delays in the Parametric Production of Photon Pairs. *Phys. Rev. Lett.*, 54(18):2011–2013, May 1985.

[16] E. S. Gómez, G. Cañas, E. Acuña, W. A. T. Nogueira, and G. Lima. Non-Gaussian-state generation certified using the Einstein-Podolsky-Rosen-steering inequality. *Phys. Rev. A*, 91(1):013801, Jan 2015.

[17] E. S. Gómez, P. Riquelme, M. A. Solís-Prosser, P. González, E. Ortega, G. B. Xavier, and G. Lima. Tunable entanglement distillation of spatially correlated down-converted photons. *Opt. Express*, 26(11):13961, May 2018.

[18] Esteban S. Gómez, Santiago Gómez, Pablo González, Gustavo Cañas, Johanna F. Barra, Aldo Delgado, Guilherme B. Xavier, Adán Cabello, Matthias Kleinmann, Tamás Vértesi, and Gustavo Lima. Device-Independent Certification of a Nonprojective Qubit Measurement. *Phys. Rev. Lett.*, 117(26):260401, Dec 2016.

[19] S. Gómez, A. Mattar, E. S. Gómez, D. Cavalcanti, O. Jiménez Farías, A. Acín, and G. Lima. Experimental nonlocality-based randomness generation with nonprojective measurements. *Phys. Rev. A*, 97(4):040102, Apr 2018.

[20] S. Gómez, A. Mattar, I. Machuca, E. S. Gómez, D. Cavalcanti, O. Jiménez Farías, A. Acín, and G. Lima. Experimental investigation of partially entangled states for device-independent randomness generation and self-testing protocols. *Phys. Rev. A*, 99(3):032108, Mar 2019.

[21] C. K. Hong and L. Mandel. Theory of parametric frequency down conversion of light. *Phys. Rev. A*, 31(4):2409–2418, apr 1985.

[22] Michael A. Nielsen and Isaac L. Chuang. *Quantum computation and quantum information*. Cambridge University Press, 2010.

[23] L. Pereira, J. J. García-Ripoll, and T. Ramos. Complete physical characterization of quantum nondemolition measurements via tomography. *Phys. Rev. Lett.*, 129:010402, Jun 2022.

[24] N. Bohr Dr. phil. I. on the constitution of atoms and molecules. *The London, Edinburgh, and Dublin Philosophical Magazine and Journal of Science*, 26(151):1–25, 1913.

[25] Bahaa E. A. Saleh and Malvin Carl. Teich. *Fundamentals of photonics.* Wiley, 2013.

[26] Fabian Steinlechner, Marta Gilaberte, Marc Jofre, Thomas Scheidl, Juan P. Torres, Valerio Pruneri, and Rupert Ursin. Efficient heralding of polarization-entangled photons from type-0 and type-II spontaneous parametric downconversion in periodically poled $KTiOPO_4$. *J. Opt. Soc. Am. B*, 31(9):2068, Sep 2014.

[27] T. Suhara. Generation of quantum-entangled twin photons by waveguide nonlinear-optic devices. *Laser Photonics Rev.*, 3(4):370–393, Jul 2009.

[28] John Meurig Thomas. The birth of X-ray crystallography. *Nature*, 491(2), Nov 2012.

[29] Sillard, Pierre and Bigot-Astruc, Marianne and Molin, Denis Few-Mode Fibers for Mode-Division-Multiplexed Systems. *Journal of Lightwave Technology*, 32(16), Aug 2019.

[30] Fulvio Flamini, Nicolò Spagnolo and Fabio Sciarrino Photonic quantum information processing: a review. *Reports on Progress in Physics*, 82(1), Nov 2018.

[31] Gisin, Nicolas. Quantum communication. *Nature Photonics*, 1(1), March 2007.

[32] Richardson, D. J. and Fini, J. M. and Nelson, L. E. Space-division multiplexing in optical fibres. *Nat. Photonics*, 7(5), May 2013.

[33] Jun Sakaguchi and Werner Klaus and Benjamin J. Puttnam and José Manuel Delgado Mendinueta and Yoshinari Awaji and Naoya Wada and Yukihiro Tsuchida and Koichi Maeda and Masateru Tadakuma and Katsunori Imamura and Ryuichi Sugizaki and Tetsuya Kobayashi and Yusaku Tottori and Masayuki Watanabe and R. V. Jensen. 19-core MCF transmission system using EDFA with shared core pumping coupled via free-space optics. *Optica Publishing Group*, 22(1), Jan 2014.

[34] Brackett, C.A. Dense wavelength division multiplexing networks: principles and applications. *IEEE Journal on Selected Areas in Communications*, 8(6), Aug 1990.

[35] T. A. Birks and I. Gris-Sánchez and S. Yerolatsitis and S. G. Leon-Saval and R. R. Thomson. The photonic lantern. *Adv. Opt. Photon.*, 7(2), Jun 2015.

[36] S. Yerolatsitis and I. Gris-Sánchez and T. A. Birks Adiabatically-tapered fiber mode multiplexers. *Opt. Express*, 7(2), Jan 2014.

[37] Berkhout, Gregorius C. G. and Lavery, Martin P. J. and Courtial, Johannes and Beijersbergen, Marco W. and Padgett, Miles J. Efficient Sorting of Orbital Angular Momentum States of Light. *Phys. Rev. Lett.*, 105(153601), Oct 2010.

[38] Kengo Watanabe and T. Saito and Katsunori Imamura and Masato Shiino. Development of fiber bundle type fan-out for multicore fiber. *2012 17th Opto-Electronics and Communications Conference*, 475-476, Jun 2012.

[39] Kaszlikowski, Dagomir and Gnaciński, Piotr and Żukowski, Marek and Miklaszewski, Wieslaw and Zeilinger, Anton. Violations of Local Realism by Two Entangled N-Dimensional Systems Are Stronger than for Two Qubits. *Phys. Rev. Lett.*, 4418-4421, Nov 2000.

[40] Neves, Leonardo and Lima, G. and Aguirre Gómez, J. G. and Monken, C. H. and Saavedra, C. and Pádua, S. Generation of Entangled States of Qudits using Twin Photons. *Phys. Rev. Lett.*, 94(10), Jun 2012.

[41] Cerf, Nicolas J. and Bourennane, Mohamed and Karlsson, Anders and Gisin, Nicolas Security of Quantum Key Distribution Using d-Level Systems. *Phys. Rev. Lett.*, 8(12), Mar 2002.

[42] Löffler, W. and Euser, T. G. and Eliel, E. R. and Scharrer, M. and Russell, P. St. J. and Woerdman, J. P Fiber Transport of Spatially Entangled Photons. *Phys. Rev. Lett.*, 8(12), Jun 2011.

[43] Cañas, G. and Vera, N. and Cariñe, J. and González, P. and Cardenas, J. and Connolly, P. W. R. and Przysiezna, A. and Gómez, E. S. and Figueroa, M. and Vallone, G. and Villoresi, P. and da Silva, T. Ferreira and Xavier, G. B. and Lima, G. High-dimensional decoy-state quantum key distribution over multicore telecommunication fibers. *Phys. Rev. A*, 96(2), Aug 2017.

[44] Acín, Antonio and Massar, Serge and Pironio, Stefano Randomness versus Nonlocality and Entanglement. *Phys. Rev. Lett.*, 108(2), March 2012.

[45] O. Nieto-Silleras, S. Pironio, and J. Silman Using complete measurement statistics for optimal device-independent randomness evaluation. *New Journal of Physics*, 16, 013035, Jan 2014.

[46] J.-D. Bancal, L. Sheridan, and V. Scarani More Randomness from the Same Data. *New Journal of Physics*, 16, 033011, Jan 2014.

[47] Gómez, S., Uzcátegui, D., Machuca, I. et al. Optimal strategy to certify quantum nonlocality. *Sci Rep*, 11, 20489, Jul 2021.

[48] M. Junge and C. Palazuelos. Large violation of Bell inequalities with low entanglement. *Comm. Math. Phys.*, 306, 3, 2011.

[49] M. Junge and C. Palazuelos. Bell nonlocality. *American Physical Society*, 86, 2,Apr 2014.

[50] P. Sheng Lin, D. Rosset, Y. Zhang, J.D. Bancal, Y. Cherng Liang, Device-independent point estimation from finite data and its application to device-independent property estimation, *Phys. Rev. A*, 97, 032309, 2018.

[51] A. Acín and L. Masanes, Certified randomness in quantum physics, *Nature*, 540, 7632, Dec 2016.

[52] N. J. Cerf, M. Bourennane, A. Karlsson, and N. Gisin, Security of Quantum Key Distribution Using d-Level Systems, *Phys. Rev. Lett.*, 88, 127902, 2002.

[53] A. Tavakoli and M. Zukowski, Higher-dimensional communication complexity problems: Classical protocols versus quantum ones based on Bell's theorem or prepare-transmit-measure schemes, *Phys. Rev. A*, 95, 042305, 2017.

[54] D. Martínez, A. Tavakoli, M. Casanova, G. Cañas, B. Marques, and G. Lima, High-Dimensional Quantum Communication Complexity beyond Strategies Based on Bell's Theorem, *Phys. Rev. Lett.*, 121, 150504, 2018.

[55] M. Araújo, F. Costa, and C. Brukner, Computational advantage from quantum-controlled ordering of gates, *Phys. Rev. Lett.*, 113, 250402, 2014.

[56] M. M. Taddei, J. Cariñe, D. Martínez, T. García, N. Guerrero, A. A. Abbott, M. Araújo, C. Branciard, E. S. Gómez, S. P. Walborn, L. Aolita, and G. Lima, Experimental computational advantage from superposition of multiple temporal orders of quantum gates, *PRX Quantum.*, 2, 010320, Feb 2021.

[57] T. Vértesi, S. Pironio, and N. Brunner, Closing the detection loophole in Bell experiments using qudits, *Phys. Rev. Lett.*, 104, 060401, 2010.

[58] D. Kaszlikowski, P. Gnacinski, M. Żukowski, W. Miklaszewski, and A. Zeilinger, Violations of Local Realism by Two Entangled N-Dimensional Systems Are Stronger than for Two Qubits, *Phys. Rev. Lett*, 85, 4418, 2000.

[59] D. Collins, S. Popescu, D. Collins, S. Popescu, N. Gisin, N. Linden, and S. Massar, Bell Inequalities for Arbitrarily High-Dimensional Systems, *Phys. Rev. Lett.*, 88, 020202, 2002.

[60] J. F. Clauserf, M. A. Horne, A. Shimony, and R. A. Holt, Proposed experiment to test separable hidden-variable theories, *Phys. Rev. Lett. A*, 23, 880, 1969.

[61] J. F. Clauser and M. A. Horne, Experimental consequences of objective local theories, *Phys. Rev. D*, 10, 526, 1974.

[62] J. Leach, M. J. Padgett, S. M. Barnett, S. Franke-Arnold, and J. Courtial, Measuring the Orbital Angular Momentum of a Single Photon, *Phys. Rev. Lett.*, 88, 257901, 2002.

[63] A. Vaziri, G. Weihs, and A. Zeilinger, , Experimental Two-Photon, Three-Dimensional Entanglement for Quantum Communication, *Phys. Rev. Lett.*, 89, 240401, 2002.

[64] N. H. Valencia, S. Goel, W. McCutcheon, H. Defienne, and M. Malik, Unscrambling Entanglement through a Complex Medium, *Nat. Phys.*, 16, 1116, 2020.

[65] J. Liu, I. Nape, Q. Wang, A. Vallés, J. Wang, and A. Forbes, Multidimensional entanglement transport through single-mode fiber, *Sci. Adv.*, 6, eaay0837, 2020.

[66] G. B. Xavier and G. Lima, Quantum information processing with space-division multiplexing optical fibres, *Commun. Phys.*, 3, 9, 2020.

[67] D. Cozzolino, D. Bacco, B. Da Lio, K. Ingerslev, Y. Ding, K. Dalgaard, P. Kristensen, M. Galili, K. Rottwitt, S. Ramachandran, and L. K. Oxenlowe, Orbital Angular Momentum States Enabling Fiber-based High-dimensional Quantum Communication, *Phys. Rev. Appl.*, 11, 064058, 2019.

[68] H. Cao, S.-C. Gao, C. Zhang, J. Wang, D.-Y. He, B.H. Liu, Z.-W. Zhou, Y.-J. Chen, Z.-H. Li, S.-Y. Yu, J. Romero, Y.-F. Huang, C.-F. Li, and G.-C. Guo, Distribution of high-dimensional orbital angular momentum entanglement over a 1 km few-mode fiber, *Optica*, 7, 232, 2020.

[69] . Da Lio, L. K. Oxenlowe, D. Bacco, D. Cozzolino, N. Biagi, T. N. Arge, E. Larsen, K. Rottwitt, Y. Ding, and A. Zavatta, Stable Transmission of High-Dimensional Quantum States over a 2-km Multicore Fiber, *IEEE J. Sel. Top. Quantum Electron.*, 24, 6400108, 2020.

[70] B. Da Lio, L. K. Oxenlowe, D. Bacco, D. Cozzolino, N. Biagi, T. N. Arge, E. Larsen, K. Rottwitt, Y. Ding, and A. Zavatta, Stable Transmission of High-Dimensional Quantum States over a 2-km Multicore Fiber, *IEEE J. Sel. Top. Quantum Electron.*, 24, 6400108, 2020.

[71] Y. Ding, D. Bacco, K. Dalgaard, X. Cai, X. Zhou, K. Rottwitt, and L. K. Oxenlowe, High-dimensional quantum key distribution based on multicore fiber using silicon photonic integrated circuits, *Quantum Inf.*, 3, 25, 2017.

[72] J. Cariñe, G. Cañas, P. Skrzypczyk, I. Supic, N. Guerrero, T. García, L. Pereira, M. Solís Prosser, G. Xavier, A. Delgado, S. Walborn, D. Cavalcanti, and G. Lima, Multi-port beamsplitters based on multi-core optical fibers for high-dimensional quantum information, *Optica*, 7, 542, 2020.

[73] H. J. Lee, S. K. Choi, and H. S. Park, Experimental Demonstration of Four-Dimensional Photonic Spatial Entanglement between Multi-core Optical Fibres, *Sci. Rep.*, 7, 4302, 2017.

[74] H. J. Lee and H. S. Park, Generation and measurement of arbitrary four-dimensional spatial entanglement between photons in multicore fibers, *Photonics Res.*, 7, 19, 2019.

[75] M. Reck, A. Zeilinger, H. J. Bernstein, and P. Bertani, Experimental Realization of Any Discrete Unitary Operator, *Phys. Rev. Lett.*, 73, 58, 1994.

[76] J. Carolan, C. Harrold, C. Sparrow, E. Martín López, N. J. Russell, J. W. Silverstone, P. J. Shadbolt, N. Matsuda, M. Oguma, M. Itoh, G. D. Marshall, M. G. Thompson, J. C. F. Matthews, T. Hashimoto, J. L. O Brien, and A. Laing, Universal linear optics, *Science*, 349, 6249, 2015.

[77] J. Wang, S. Paesani, Y. Ding, R. Santagati, P. Skrzypczyk, A. Salavrakos, J. Tura, R. Augusiak, L. Mancinska, D. Bacco, D. Bonneau, J. W. Silverstone, Q. Gong, A. Acín, K. Rottwitt, L. K. Oxenlowe, J. L., O Brien, A. Laing, and M. G. Thompson Multidimensional quantum entanglement with large-scale integrated optics, *Science*, 360, 285, 2018.

[78] C. Schaeff, R. Polster, R. Lapkiewicz, R. Fickler, S. Ramelow, and A. Zeilinger Scalable fiber integrated source for higher-dimensional path-entangled photonic quNits, *Opt. Express*, 20, 16145, 2012.

[79] L. Gan, R. Wang, D. Liu, L. Duan, S. Liu, S. Fu, B. Li, Z. Feng, H. Wei, W. Tong, P. Shum, and M. Tang Spatial-division multiplexed Mach-Zehnder interferometers in heterogeneous multicore fiber for multiparameter measurement, *IEEE Photonics J.*, 8, 7800908, 2016.

[80] M. Yu Saygin, I. V. Kondratyev, I. V. Dyakonov, S. A. Mironov, S. S. Straupe, and S. P. Kulik, Robust Architecture for Programmable Universal Unitaries, *Phys. Rev. Lett.*, 124, 010501, 2020.

[81] L. Pereira, A. Rojas, G. Cañas, G. Lima, A. Delgado, and A. Cabello, Universal multi-port interferometers with minimal optical depth, *arXiv:2002.01371*, 2020.

[82] D. N. Klyshko, Scattering of light in a medium with nonlinear polarizability, *Sov. Phys. JETP*, 28, 522, 1969.

[83] D. C. Burnham and D. L. Weinberg, Observation of simultaneity in parametric production of optical photon pairs, *Phys. Rev. Lett.*, 25, 84, 1970.

[84] A. V. Burlakov, M. V. Chekhova, D. N. Klyshko, S. P. Kulik, A. N. Penin, Y. H. Shih, and D. V. Strekalov, Interference effects in spontaneous two-photon parametric scattering from two macroscopic regions, *Phys. Rev. A At. Mol. Opt. Phys.*, 56, 3214, 1997.

[85] Sergi Garcia, Mario Urena, and Ivana Gasulla, Bending and twisting effects on multicore fiber differential group delay, *Optics Express.*, 27, 31290, 2019.

[86] A. Bhattacharyya, *Bulletin of the Calcutta Mathematical Society.*, 35, 99, 1943.

[87] A. J. Gutiérrez-Esparza, W. M. Pimenta, B. Marques, A. A. Matoso, J. Sperling, W. Vogel, and S. Pádua, Detection of nonlocal superpositions, *Phys. Rev. A*, 90, 032328, 2014.

[88] J. Bavaresco, N. Herrera Valencia, C. Klöckl, M. Pivoluska, P. Erker, N. Friis, M. Malik, and M. Huber, Measurements in two bases are sufficient for certifying high-dimensional entanglementt, *Nat. Phys.*, 14, 1032, 2018.

[89] H. M. Wiseman, S. J. Jones, and A. C. Doherty, Steering, entanglement, nonlocality, and the Einstein- Podolsky-Rosen paradox, *Phys. Rev. Lett.*, 98, 140402, 2007.

[90] C. Branciard, E. G. Cavalcanti, S. P. Walborn, V. Scarani, and H. M. Wiseman, One-sided device-independent quantum key distribution: Security, feasibility, and the connection with steering, *Phys. Rev. A - At. Mol. Opt. Phys.*, 85, 010301, 2012.

[91] Y. Z. Law, L. P. Thinh, J. D. Bancal, and V. Scarani, Quantum randomness extraction for various levels of characterization of the devices, . *Phys. A Math. Theor.*, 47, 424028, 2014.

[92] E. Passaro, D. Cavalcanti, P. Skrzypczyk, and A. Acín, Optimal randomness certification in the quantum steering and prepare-and-measure scenarios, *New J. Phys.*, 17, 113010, 2015.

[93] A. Máttar, P. Skrzypczyk, G. H. Aguilar, R. V. Nery, P. H. S. Ribeiro, S. P. Walborn, and D. Cavalcanti, Experimental multipartite entanglement and randomness certification of the W state in the quantum steering scenario, *Quantum Sci. Technol.*, 2, 015011, 2017.

[94] J. Schneeloch, C. J. Broadbent, S. P. Walborn, E. G. Cavalcanti, and J. C. Howell, Einstein-Podolsky-Rosen steering inequalities from entropic uncertainty relations, *Phys. Rev. A*, 87, 062103, 2018.

[95] Kwiat, Paul G. and Waks, Edo and White, Andrew G. and Appelbaum, Ian and Eberhard, Philippe H., Ultrabright source of polarization-entangled photons, *Phys. Rev. A*, 60, 2, 1999.

[96] M. A. Ciampini, N. Spagnolo, C. Vitelli, L. Pezzé, A. Smerzi, and F. Sciarrino, Quantum-enhanced multi-parameter estimation in multiarm interferometers, *Sci. Rep.*, 6, 28881, 2016.

[97] Mears, R. J., Reekie, L., Jauncey, I. M. and Payne, D. N., Low-noise Erbium-doped fiber amplifier at $1.54\mu m$, *Electron. Lett.*, 23, 1026-1028, 1987.

[98] Brackett, C. A., Dense wavelength division multiplexing networks: principles and applications, *IEEE J. Sel. Areas Commun.*, 8, 948-964, 1990.

[99] Agrawal, G. P., *Fiber-optic communication systems, 3rd edn (Wiley, New York)*, 2202.